Cascades of turbulent kinetic energy and multicomponent scalars in a momentum-scalar coupling turbulence driven by multiple mechanisms under homogeneous and isotropic hypotheses

Wei Zhao *

State Key Laboratory of Photon-Technology in Western China Energy, International Scientific and Technological Cooperation Base of Photoelectric Technology and Functional Materials and Application, Laboratory of Optoelectronic Technology of Shaanxi Province, Institute of Photonics and Photon-technology, Northwest University, Xi'an 710127, China

(Received 7 December 2023; accepted 8 August 2024; published 26 August 2024)

Momentum-scalar coupling turbulence, a phenomenon observed in both natural and engineering contexts, involves the intricate interaction between multicomponent scalars and multiscale forces (i.e., multiple coupling mechanisms), resulting in a wide array of manifestations. Despite its importance, limited research has been conducted to comprehend the influence of these multicomponent and multiple coupling mechanisms on turbulence cascades. Hence, this study aims to provide a preliminary and theoretical exploration into how these multiple coupling mechanisms govern the cascades of turbulent kinetic energy and multicomponent scalars. To simplify the mathematical analysis, homogeneous and isotropic hypotheses of flow field have been applied. The key findings of this study can be summarized as follows. The first is validation of quad-cascade processes. The second is an examination of various cases involving single scalar components but multiple coupling mechanisms. Of particular interest is the coexistence of buoyancy-driven turbulence and electrokinetic turbulence, which introduces a new variable flux (VF) subrange resulting from their nonlinear interaction. Another extension considers an exponential modulation function, equivalent to the coexistence of multiple coupling mechanisms acting on a single scalar. The study identifies two new VF subranges. Third, binary scalar components and coupling mechanisms are investigated, indicating coupling mechanisms with significantly different strengths that can also induce complex interactions and new VF subranges. Fourth is the complexity when three or more different scalar components and coupling mechanisms coexist simultaneously: with the exception of certain special cases, closure of the problem becomes unattainable. This highlights the challenges inherent in addressing the simultaneous presence of multiple scalar components and coupling mechanisms. This research endeavor illuminates the theoretical understanding of the diverse scaling properties observed in momentum-scalar coupling turbulence across different scenarios.

DOI: 10.1103/PhysRevFluids.9.084610

I. INTRODUCTION

Turbulence is pervasive in nature and engineering, arising from various physical mechanisms such as hydrodynamics, thermal convection [1], electrohydrodynamics [2], magnetohydrodynamics [3,4], and even in quantum [5,6] and biological [7] systems. Turbulent transport involves diverse scalars such as temperature [8,9], salinity [10,11], electric conductivity [12–14], and permittivity

*Contact author: zwbayern@nwu.edu.cn

[15,16], among others such as magnetic susceptibility [17] and chemical components [18,19]. These scalars display a multiscale distribution in wavenumber space and can generate external multiscale forces through different physical mechanisms, driving the flow towards a state of turbulence through a feedback mechanism.

In the real world, it is rare for just a single scalar or physical mechanism to be isolated. Instead, the coexistence of multicomponent scalars and multiphysical interactions is the normal state. In the atmosphere, for example, buoyancy-driven flow, electrohydrodynamic flow due to spatial electric charge distribution [2,20], and magnetohydrodynamic flow influenced by the Earth's magnetic field [21] all occur concurrently. Buoyancy-driven turbulence—which includes thermal convection, stratified turbulence, and boundary layers—is a key mechanism in atmospheric evolution on scales up to hundreds of kilometers. The atmosphere contains various electric media such as charged species, gases with differing moisture levels, droplets, and dust clouds, leading to spatial and temporal variations in electric conductivity and permittivity. Given that the atmosphere is not electrically neutral and can experience electric fields as strong as 10^6 V/m during thunderstorms, electrohydrodynamic (EHD) and electrokinetic (EK) turbulence—both driven by electric body force (EBF)—are also inevitable in atmospheric flow up to kilometer scales. Additionally, whenever charged species are unevenly distributed, deviations from electrical neutrality arise locally. This scenario leads to the flow carrying nonuniform charges, resulting in electric currents. Under the Earth's magnetic field, these currents produce Lorentz forces (LFs), necessitating the presence of magnetohydrodynamic (MHD) effects. Thus, buoyancy-driven turbulence, EBF-driven turbulence, and LF-driven (MHD) turbulence coexist and can collectively dictate wind evolution in both large and small scales.

Similar examples of turbulence driven by multiscale forces exist elsewhere. In the ocean, temperature and salinity jointly affect flows on various scales. At the core of the Earth [22], the combination of high and uneven temperatures with ferromagnetism can mutually impact the dynamics of the outer liquid core. Moreover, in fields like chemical engineering and combustion, multicomponent scalar systems are also prevalent [23]. These scenarios highlight the intricate interplay and importance of understanding multiscalar and multiphysical interactions in turbulent systems.

Unfortunately, most theoretical and numerical researches study the "real-world turbulence" [24] by focusing on a single scalar and one dominant physical mechanism, such as buoyancy or electrostatic influence. A paradigm of momentum-scalar coupled turbulent flow—buoyancy-driven turbulence—has attracted significant attention over the past several decades. Obukhov's work [25] laid the theoretical groundwork for understanding the inertial subrange of passive scalar transport in turbulence characterized by high Reynolds numbers. Subsequently, Bolgiano [26] and Obukhov [27] independently introduced the Bolgiano-Obukhov (BO59) law [28]. According to their predictions, in the subrange primarily influenced by buoyancy effects arising from density or temperature variations, the spectra of turbulent kinetic energy and scalar variance demonstrate specific characteristics as

$$E_u(k) \sim k^{-\frac{11}{5}} \quad \text{and} \quad E_s(k) \sim k^{-\frac{7}{5}}. \tag{1}$$

The buoyancy-dominant subrange described by the BO59 law represents a region characterized by partially variable flux; within this context, the flux of scalar variance remains constant while that of turbulent kinetic energy does not. Since the influence of buoyancy decays rapidly along wavenumber, the buoyancy-dominant subrange occurs at the lower-wavenumber side of the inertial subrange. In 2000, Niemela *et al.* [9] first observed slopes of $-\frac{11}{5}$ and $-\frac{7}{5}$ in the spectra of turbulent kinetic energy and temperature variance, respectively. Subsequently, several researchers [29–31] claimed that the BO59 law can be predicted through numerical simulations across various scenarios. However, both numerical and experimental investigations still lack convincing results regarding the BO59 law. For a more comprehensive review of buoyancy-driven turbulence, please refer to Ref. [32]. In an effort to address this issue, Alam *et al.* [33] revisited the BO59 law and attempted to explain why its observation has not been successful. Notably, their work provided

numerical observations of a novel scaling subrange featuring nonconstant flux of scalar variance and constant flux of kinetic energy, which, in my opinion, constitutes their most significant contribution. Regrettably, this observation did not receive much attention at the time.

Electrokinetic turbulence pertains to a turbulence phenomenon primarily observed in electrolyte solutions with nonuniform electric properties (such as electric conductivity or permittivity), driven by EBF through electrostatic effects. Regarding EK turbulence, Zhao and Wang [16,34] have developed a series of theoretical frameworks aimed at elucidating the transport of turbulent kinetic energy and scalar variance. Based on a hypothesis involving a constant flux of scalar variance (electric conductivity or permittivity) with a nonconstant flux of kinetic energy, they predicted that the spectra of turbulent kinetic energy and scalar variance would exhibit

$$E_u(k) \sim k^{-\frac{7}{5}} \quad \text{and} \quad E_s(k) \sim k^{-\frac{9}{5}}. \tag{2}$$

Furthermore, it was predicted that in EK turbulence, where the EBF becomes dominant at small scales, the subrange where the cascades of turbulent kinetic energy and scalar variance are influenced by the EBF should occur at the higher-wavenumber range of the inertial subrange. As a result, EK turbulence is characterized by a bidirectional cascade of turbulent kinetic energy and a direct cascade of scalar variance [35]. This represents another significant difference between buoyancy-driven turbulence and EK turbulence.

In magnetohydrodynamic turbulence, numerous theories have been proposed over the past 60 years. Iroshinikov [36] and Kraichnan [37] separately introduced the Iroshinikov-Kraichnan spectrum for MHD turbulence by considering the influence of the Alfvén effect on the cascade of turbulent kinetic energy [38]. According to their theory, the energy spectrum $E_u(k)$ in the inertial subrange of MHD turbulence follows a power law of $k^{-3/2}$, deviating from the classical Kolmogorov $-\frac{5}{3}$ law, even though the latter is more commonly observed in experimental data [39,40] and numerical simulations of MHD turbulence [38,41]. In contrast, the Iroshinikov-Kraichnan theory was numerically supported by Eyink *et al.* [4] when considering a Richardson dispersion, besides the Alfvén effect. Further theoretical models, such as the anisotropic MHD energy spectrum $E_u(k) \sim k^{-5/2}$, have also been proposed for the inertial subrange of anisotropic MHD turbulence [38]. Moreover, experimental investigations [21] have revealed a wider array of scaling behaviors. Despite these advances, the research focus has largely been on the form of the inertial subrange, not so much on the more intricate subrange where the Lorentz force takes precedence in the cascades of turbulent kinetic energy and related scalar fields like magnetic conductivity. Verma [42] provides an extensive overview of recent developments in this field.

As can be seen above, the current discourse on turbulence often follows a reductionist approach, suggesting that a single primary mechanism largely governs these phenomena, which can overlook the inherent complexity of such systems. In the physical and life sciences [43], the concept of emergence acknowledges that multifaceted, highly nonlinear systems exhibit behaviors that cannot be attributed solely to one dominant mechanism, ignoring the distinction between primary and secondary effects. This concept, highlighted in Anderson's seminal paper "More is Different" [44], emphasizes the novelty arising from complex interactions across different scales.

Turbulence is a prime example of a highly nonlinear system where isolating individual components and coupling mechanisms is often impractical, especially in fields like engineering, meteorology, oceanography, and astrophysics. In EK or EHD turbulence, the interplay of external electric fields with fluids produces both electrostatic forces and electrothermal effects, the latter leading to buoyancy through temperature variations. Traditionally, electrostatically induced EK turbulence is considered the primary factor. However, the influence of electrothermal effects on overall turbulence is not well understood. The presence of such multidimensional coupling mechanisms can lead to unexpected and novel emergent behaviors.

Despite the significance of this multifaceted interplay in turbulent systems, research on the cascades of turbulent kinetic energy and scalar fields influenced by multiple mechanisms is lacking. This study aims to explore the interplay among the physical mechanisms governing the cascade

processes of turbulent kinetic energy and multicomponent scalars. It reveals that interactions between coupling mechanisms of distinct strengths can generate new scaling behaviors in the spectra of turbulent kinetic energy and the variances of two scalar quantities.

II. THEORY

Most theoretical models to date have focused on the inertial subrange (e.g., Kolmogorov's 1941 law and the Obukhov-Corrsin law), the constant scalar flux subrange (e.g., the BO59 law and Zhao and Wang's model [16,34,45]), and the variable flux (VF) subrange (e.g., Verma [42] and Shur-Lumley models [46]). In 2022, inspired by Alam *et al.*'s investigation of stably stratified turbulence [33], Zhao [47] developed a model for momentum-scalar coupling turbulence based on the fluxes of turbulent kinetic energy (Π_u) and scalar variance (Π_s).

This model employed a multiscale force of $\nabla^a s'$ type (also see Ref. [45]) to describe the coupling relationship between momentum and scalar fluctuations (s'). It theoretically predicted a quad-cascade process involving turbulent kinetic energy and scalar variance, covering the inertial subrange, constant energy flux (constant-Π_u) subrange, constant scalar flux (constant-Π_s) subrange, and VF subrange. Zhao's model [47] provides a comprehensive framework for studying complex momentum-scalar coupling turbulence with multiple scalar components and coupling mechanisms, encompassing various phenomena such as buoyancy-driven flow, electrokinetic flow, and magneto-hydrodynamic flow with differing a values.

A. Conservative law by the fluxes of turbulent kinetic energy and multicomponent scalars

In this investigation, based on Zhao's model [47], a flux model for momentum-scalar coupling turbulence with multicomponent scalars and multiple coupling mechanisms is studied theoretically and numerically. A three-dimensional model has been considered. The governing equations are expressed as follows:

$$\frac{D\boldsymbol{u}}{Dt} = -\frac{1}{\rho}\nabla p + \nu\Delta u + \sum_{i=1}^{i\max} \boldsymbol{M_i}\mathfrak{D}^{\frac{\beta_i}{4}} s'_i, \tag{3a}$$

$$\frac{Ds'_1}{Dt} = -\boldsymbol{N_1}\cdot\boldsymbol{u} + D_{f,1}\Delta s'_1$$

$$\vdots$$

$$\frac{Ds'_i}{Dt} = -\boldsymbol{N}_i\cdot\boldsymbol{u} + D_{f,i}\Delta s'_i$$

$$\vdots$$

$$\frac{Ds'_{i\max}}{Dt} = -\boldsymbol{N_{i\,max}}\cdot\boldsymbol{u} + D_{f,i\max}\Delta s'_{i\max}, \tag{3b}$$

$$\nabla\cdot\boldsymbol{u} = 0, \tag{3c}$$

where ρ is the referenced fluid density, $\boldsymbol{u}$ denotes the velocity vector, p is pressure, and s'_i is the fluctuation of the ith scalar component. $D/Dt = d/dt + \boldsymbol{u}\cdot\nabla$ is material derivative. In this paper, $\mathfrak{D} = \Delta^2$, with $\Delta = \nabla\cdot\nabla$ being a Laplacian operator. $\mathfrak{D}^{\beta_i/4}s'_i$ denotes the fractional derivation on s'_i with orders $\beta_i/4$, respectively. $\boldsymbol{M_i}\mathfrak{D}^{\beta_i/4}s'_i$ is the multiscale force related to the ith scalar field s'_i [45,47], with $\boldsymbol{M_i}$ being the dimensional vector associated with the ith physical field. $\boldsymbol{N_i} = \nabla\bar{s_i}$ is the gradient of the mean field $(\bar{\cdot})$ with respect to the ith scalar s_i. It characterizes the strength of the mean scalar gradient that can be provided from the background flow. ν and $D_{f,i}$ are the kinematic viscosity and diffusivity of the ith scalar, respectively. The assumption ($\nabla^2\bar{s}_i \ll \nabla^2 s'_i$) is made for the model.

For example, in buoyancy-driven turbulence, it is approximately $\beta_i = 0$. s'_i can be either temperature fluctuations with $\boldsymbol{M_i} = \alpha g \hat{\boldsymbol{z}}$ and $\boldsymbol{N_i} = \boldsymbol{\nabla} \bar{T}$, or density fluctuations with $\boldsymbol{M_i} = \boldsymbol{N_i} = -f_{\mathrm{VB}} \hat{\boldsymbol{z}}$, respectively. Here, α is the thermal expansion coefficient, g is gravity acceleration, $\hat{\boldsymbol{z}}$ is the inverse direction of gravity, $\bar{T}$ is the mean field of temperature (T), and $f_{\mathrm{VB}} = \sqrt{\frac{g}{\bar{\rho}} |\frac{d\rho_0}{dz}|}$ is Väisälä-Brunt frequency. ρ_0 and $\bar{\rho}$ are background density and mean density, respectively [33,42]. In an electrokinetic turbulence generated by electrostatic force, when the electric field (E) is in the y direction ($\hat{\boldsymbol{y}}$) that is perpendicular to the initial interface of electric conductivity (σ), as investigated by Wang *et al.* [12,13], it is approximately $\beta_i = 1$, with $\boldsymbol{M_i} = -\varepsilon E^2 \hat{\boldsymbol{y}} / \rho \bar{\sigma}$ and $\boldsymbol{N_i} = \boldsymbol{\nabla} \bar{\sigma}$. Here, ε is electric permittivity and $\bar{\sigma}$ is the mean field of electric conductivity [47].

In this model, two hypotheses have been made to simplify the analysis:

(1) All scalar components are assumed to be independent and nonreactive. This is analogous to the well-known Boussinesq approximation [32,48]. For instance, in buoyancy-driven turbulence, buoyancy can result from stratifications of temperature, density (different materials), and salinity, which can be treated as being independent of each other. Similarly, in electrokinetic turbulence in an electrolyte solution with different free ions (e.g., Na^+, Ca^{2+}, and Cl^-), ions are considered independent and nonreactive.

(2) Turbulent flow is approximated as homogeneous and isotropic. This approximation is common in many classical turbulent models, such as the Kolmogorov 1941 (K41) law, Obukhov-Corrsin law, and BO59 law for stably stratified turbulence, as well as the Zhao-Wang model [16,34] for electrokinetic turbulence. This hypothesis is partially supported by studies such as that by Nath *et al.* [49] in turbulent thermal convection and that by Kumar *et al.* [29] in stably stratified turbulence.

In Fourier space, let $E_u(\boldsymbol{k}) = \frac{1}{2}|\boldsymbol{u}(\boldsymbol{k})|^2$ and $E_{s,i}(\boldsymbol{k}) = \frac{1}{2}|s'_i(\boldsymbol{k})|^2$ be the modal turbulent kinetic energy and ith scalar variance. Equations (3) can be rewritten as [24,42,50]

$$\frac{d}{dt} E_u(\boldsymbol{k}) = T_u(\boldsymbol{k}) - D_u(\boldsymbol{k}) + \sum_{i=1}^{i\max} F_{s,i}(\boldsymbol{k}), \tag{4a}$$

$$\frac{d}{dt} E_{s,i}(\boldsymbol{k}) = T_{s,i}(\boldsymbol{k}) - D_{s,i}(\boldsymbol{k}) - F_{A,i}(\boldsymbol{k}), \tag{4b}$$

$$k_l u_l(k) = 0, \tag{4c}$$

with

$$T_u(\boldsymbol{k}) = \mathrm{Im}\left[\int k_l \widehat{u_l}(n) \widehat{u_q}(m) \widehat{u_q^*}(k) dk^3 \right], \tag{5a}$$

$$T_{s,i}(\boldsymbol{k}) = \mathrm{Im}\left[\int k_l \widehat{u_l}(n) \widehat{s_i'}(m) \widehat{s_i'^*}(k) dn^3 \right], \tag{5b}$$

$$F_{s,i}(\boldsymbol{k}) = \mathrm{Re}\left[k^{\beta_i} M_{i_q} \widehat{s_i'}(k) \widehat{u_q^*}(k) \right], \tag{5c}$$

$$F_{A,i}(\boldsymbol{k}) = \mathrm{Re}\left[N_{i_q} \widehat{s_i'}(k) \widehat{u_q^*}(k) \right], \tag{5d}$$

$$D_u(\boldsymbol{k}) = 2\nu k^2 E_u(\boldsymbol{k}), \tag{5e}$$

$$D_{s,i}(\boldsymbol{k}) = 2D_{f,i} k^2 E_{s,i}(\boldsymbol{k}), \tag{5f}$$

where Re and Im represent the real and imaginary parts of the quantity. $\boldsymbol{k} = k_l \widehat{x_l}$ and $k = |\boldsymbol{k}| = (k_l k_l)^{1/2}$, with k_l being the wavenumber component in the lth direction (denoted by $\widehat{x_l}$). The wavenumbers have a relation of $\boldsymbol{k} = \boldsymbol{m} + \boldsymbol{n}$. $\widehat{u_q}$ is the Fourier transform of the qth directional component of $\boldsymbol{u}$. $\widehat{s_i'}$ is the Fourier transform of s'_i. The asterisk represents a complex conjugate. $T_u(\boldsymbol{k})$ and $D_u(\boldsymbol{k})$ are the nonlinear turbulent kinetic energy transfer rate and dissipation rate, respectively. $T_{s,i}(\boldsymbol{k})$ and $D_{s,i}(\boldsymbol{k})$ are the nonlinear transfer rate of the ith scalar variance and scalar dissipation rate, respectively. $F_{s,i}(\boldsymbol{k})$ denotes the energy feeding rate by the multiscale force due to the ith scalar field and $F_{A,i}(\boldsymbol{k})$ is the ith scalar feeding rate by bulk components.

Assuming the velocity and scalar fields are homogeneous and isotropic, in a spherical shell around k with a thickness of dk in the wavenumber space, Eqs. (4a) and (4b) become [51]

$$\sum_{k<|\boldsymbol{k}'|\leqslant k+dk}\frac{d}{dt}E_u(\boldsymbol{k}')=\sum_{k<|\boldsymbol{k}'|\leqslant k+dk}\left[T_u(\boldsymbol{k}')+\sum_{i=1}^{i\max}F_{s,i}(\boldsymbol{k}')-D_u(\boldsymbol{k}')\right], \tag{6a}$$

$$\sum_{k<|\boldsymbol{k}'|\leqslant k+dk}\frac{d}{dt}E_{s,i}(\boldsymbol{k}')=\sum_{k<|\boldsymbol{k}'|\leqslant k+dk}[T_{s,i}(\boldsymbol{k}')-F_{A,i}(\boldsymbol{k}')-D_{s,i}(\boldsymbol{k}')]. \tag{6b}$$

Since the flux of turbulent kinetic energy $\Pi_u(k)=-\sum_{|\boldsymbol{k}'|\leqslant k}T_u(\boldsymbol{k}')$ and the flux of scalar variance $\Pi_{s,i}(k)=-\sum_{|\boldsymbol{k}'|\leqslant k}T_{s,i}(\boldsymbol{k}')$ [33,42,47], we can define

$$d\Pi_u(k)=-\sum_{k\leqslant|\boldsymbol{k}'|\leqslant k+dk}T_u(\boldsymbol{k}'), \tag{7a}$$

$$d\Pi_{s,i}(k)=-\sum_{k\leqslant|\boldsymbol{k}'|\leqslant k+dk}T_{s,i}(\boldsymbol{k}'), \tag{7b}$$

$$E_u(k)dk=\sum_{k<|\boldsymbol{k}'|\leqslant k+dk}E_u(\boldsymbol{k}'), \tag{7c}$$

$$E_{s,i}(k)dk=\sum_{k<|\boldsymbol{k}'|\leqslant k+dk}E_{s,i}(\boldsymbol{k}'), \tag{7d}$$

$$F_{s,i}(k)dk=\sum_{k<|\boldsymbol{k}'|\leqslant k+dk}F_{s,i}(\boldsymbol{k}'), \tag{7e}$$

$$F_{A,i}(k)dk=\sum_{k<|\boldsymbol{k}'|\leqslant k+dk}F_{A,i}(\boldsymbol{k}'), \tag{7f}$$

$$D_u(k)dk=\sum_{k<|\boldsymbol{k}'|\leqslant k+dk}D_u(\boldsymbol{k}'), \tag{7g}$$

$$D_{s,i}(k)dk=\sum_{k<|\boldsymbol{k}'|\leqslant k+dk}D_{s,i}(\boldsymbol{k}'), \tag{7h}$$

where $E_u(k)$ and $E_{s,i}(k)$ are the averaged power spectra of turbulent kinetic energy and the ith scalar variance over the spherical shell, $F_{s,i}(k)$ is the energy feeding rate by multiscale force due to the ith scalar field at wavenumber k, $F_{A,i}(k)$ is the ith scalar feeding rate at wavenumber k, and D_u and $D_{s,i}$ are dissipation terms at wavenumber k, respectively. After substituting Eqs. (7a)–(7h) into Eqs. (6a) and (6b), considering the flow is statistically equilibrium, and letting d$k\to 0$, the following is obtained:

$$\frac{d}{dk}\Pi_u(k)=\sum_{i=1}^{i\max}F_{s,i}(k)-D_u(k), \tag{8a}$$

$$\frac{d}{dk}\Pi_{s,i}(k)=-F_{A,i}(k)-D_{s,i}(k), \tag{8b}$$

where

$$F_{s,i}(k)=\mathrm{Re}\left[k^{\beta_i}M_{i_q}\widehat{s_i'}(k)\widehat{u_q^*}(k)\right], \tag{9a}$$

$$F_{A,i}(k)=\mathrm{Re}\left[N_{i_q}\widehat{s_i'}(k)\widehat{u_q^*}(k)\right], \tag{9b}$$

$$D_u(k)=2\nu k^2E_u(k), \tag{9c}$$

$$D_{s,i}(k)=2D_{f,i}k^2E_{s,i}(k). \tag{9d}$$

Thus, if $\boldsymbol{M_i}$ is parallel to $\boldsymbol{N_i}$,

$$F_{s,i}(k) - \frac{M_i}{N_i} F_{A,i}(k) k^{\beta_i} = 0, \tag{10}$$

where $M_i = |\boldsymbol{M_i}|$ and $N_i = |\boldsymbol{N_i}|$, respectively.

B. Inertial subrange

In the inertial subrange, where the influence of multiscale forcing and dissipation is negligible, Eqs. (8a) and (8b) become

$$\frac{d}{dk}\Pi_u(k) = 0, \tag{11a}$$

$$\frac{d}{dk}\Pi_{s,i}(k) = 0, \tag{11b}$$

or

$$\Pi_u(k) = \text{const along } k,$$

$$\Pi_{s,i}(k) = \text{const along } k.$$

In the flow region far from boundary layers, known as the bulk region, the statistical features can significantly differ from those in the boundary layers, as seen in buoyancy-driven turbulence [32]. In the bulk region, the following relationship can be established [33,47]:

$$E_u(k) = u_k^2/k \sim k^{\xi_u}, \tag{12a}$$

$$E_{s,i}(k) = s_{k,i}^2/k \sim k^{\xi_{s,i}}, \tag{12b}$$

$$\Pi_u(k) = k u_k^3 \sim k^{\lambda_u}, \tag{12c}$$

$$\Pi_{s,i}(k) = k s_{k,i}^2 u_k \sim k^{\lambda_{s,i}}, \tag{12d}$$

where ξ_u, $\xi_{s,i}$, λ_u, and $\lambda_{s,i}$ denote the scaling exponents of E_u, $E_{s,i}$, Π_u, and $\Pi_{s,i}$, respectively. u_k and $s_{k,i}$ represent the velocity and ith scalar components in k space. It can be deduced that

$$E_u^{3/2} k^{5/2} = \text{const along } k, \tag{13a}$$

$$E_{s,i} E_u^{1/2} k^{5/2} = \text{const along } k. \tag{13b}$$

Thereafter, the celebrated K41 law and Obukhov-Corrsin law for inertial subrange have been derived, with $\xi_u = \xi_{s,i} = -5/3$. Considering Eq. (11a) is a direct consequence of the Navier-Stokes equation, if the Navier-Stokes equation has smooth and power-law solutions in spectral space, the $k^{-5/3}$ spectrum related to the K41 law must be one of them. From these equations, it can be inferred that, in the inertial subrange, there must be constant Π_u and $\Pi_{s,i}$ for all the scalars, which are independent of each other. Each scalar will exhibit a $-\frac{5}{3}$ slope in the spectra of scalar variance, although with different spectral intensities.

C. Conservative law in the MFD subrange

From Eq. (9a), it is evident that the multiscale force depends not only on the strong coupling between the scalar and velocity spectra, but is also modulated by k^{β_i}, where β_i is primarily determined by the physical mechanism. The influence of the work input by the multiscale force extends across a wide subrange in the spectral space, rather than being limited to a single wavenumber (or frequency) or a narrow spectral band. This is why the forcing term in Eq. (3a) is referred to as a multiscale force. In the subrange where the transports of turbulent kinetic energy and scalar variance are dominated by the multiscale force, known as the multiscale-force-dominated (MFD) subrange, the dissipation

terms of turbulent kinetic energy and scalar variance are neglected. As a result, Eqs. (8a) and (8b) simplify to

$$\frac{d}{dk}\Pi_u(k) = \sum_{i=1}^{i\max} F_{s,i}(k), \tag{14a}$$

$$\frac{d}{dk}\Pi_{s,i}(k) = -F_{A,i}(k). \tag{14b}$$

Combining Eq. (10) and Eqs. (14a) and (14b), a conservation law is thus obtained:

$$\frac{d}{dk}\Pi_u(k) + \sum_{i=1}^{i\max} \frac{M_i}{N_i} k^{\beta_i} \frac{d}{dk}\Pi_{s,i}(k) = 0. \tag{15}$$

It can be seen that Eqs. (11a) and (12b) are the special solutions of Eq. (15) as well. Therefore, the scenarios of Kolmogorov [52,53], and Obukhov and Corrsin's [25,54] theories, have been unified into this model. After substituting Eqs. (12c) and (12d) into Eq. (15), the following is obtained:

$$\frac{d}{dk} k u_k^3 + \sum_{i=1}^{i\max} \frac{M_i}{N_i} k^{\beta_i} \frac{d}{dk} k s_{k,i}^2 u_k = 0. \tag{16}$$

If u_k is nontrivial, Eq. (16) can be rewritten by multiplying u_k as

$$u_k \frac{d}{dk} k u_k^3 + k u_k^2 \sum_{i=1}^{i\max} \frac{M_i}{N_i} k^{\beta_i} \frac{d}{dk} s_{k,i}^2 + \left(\sum_{i=1}^{i\max} \frac{M_i}{N_i} k^{\beta_i} s_{k,i}^2 \right) u_k \frac{d}{dk} k u_k = 0. \tag{17}$$

Given that in the MFD subrange, the flow is propelled by the $\sum_{i=1}^{i\max} \boldsymbol{M_i} \mathfrak{D}^{\beta_i/4} s_i'$-type force, as expressed in Eq. (3a), the convection term is balanced by the volume force. Thus, another relationship that connects u_k and $s_{k,i}$ is established dimensionally as

$$k u_k^2 = \sum_{i=1}^{i\max} k^{\beta_i} M_i s_{k,i}. \tag{18}$$

Subsequently, by substituting Eq. (18) into Eq. (17) with simple mathematical processing, the following is obtained:

$$\sum_{j=1}^{i\max} \sum_{i=1}^{i\max} M_i M_j \left[\frac{3}{2} k^{\beta_i+\beta_j-1} s_{k,i} \left(\frac{d}{dk} s_{k,j} \right) + \frac{1}{2} (3\beta_j - 1) k^{\beta_i+\beta_j-2} s_{k,i} s_{k,j} + \frac{2}{N_j} k^{\beta_i+\beta_j} s_{k,i} s_{k,j} \left(\frac{d}{dk} s_{k,j} \right) \right.$$
$$\left. + \frac{\beta_j + 1}{2N_i} k^{\beta_i+\beta_j-1} s_{k,j} s_{k,i}^2 + \frac{1}{2N_i} k^{\beta_i+\beta_j} s_{k,i}^2 \left(\frac{d}{dk} s_{k,j} \right) \right] = 0. \tag{19}$$

Since $k^{\beta_i+\beta_j-2} s_{k,i}$ is nontrivial, finally Eq. (19) becomes

$$\sum_{j=1}^{i\max} \sum_{i=1}^{i\max} F_{ij} = 0 \tag{20}$$

with

$$F_{ij} = M_i M_j \left[\left(\frac{3}{2} k + \frac{2}{N_j} k^2 s_{k,j} + \frac{1}{2N_i} k^2 s_{k,i} \right) \left(\frac{d}{dk} s_{k,j} \right) + \frac{1}{2} (3\beta_j - 1) s_{k,j} + \frac{\beta_j + 1}{2N_i} k s_{k,i} s_{k,j} \right]. \tag{21}$$

F_{ij} represents the interaction between the ith scalar and its corresponding coupling mechanism with the jth one. In a turbulent system with $i\max \geqslant 2$, e.g., scalar A and B or their coupling mechanisms, altering their indices does not alter the underlying physics or observations. In other words,

the cascades of turbulent kinetic energy and scalar variances remain unaffected. Consequently, a corollary is proposed as follows.

Corollary. F_{ij} is invariant when switching i and j, i.e., $F_{ij} = F_{ji}$; accordingly,

$$\frac{3}{2}k\frac{d}{dk}(s_{k,j} - s_{k,i}) + k^2\frac{d}{dk}\left(\frac{s_{k,j}^2}{N_j} - \frac{s_{k,i}^2}{N_i}\right) + \left(\frac{1}{2N_i}k^2 s_{k,i}\frac{d}{dk}s_{k,j} - \frac{1}{2N_j}k^2 s_{k,j}\frac{d}{dk}s_{k,i}\right)$$
$$+\frac{3}{2}(\beta_j s_{k,j} - \beta_i s_{k,i}) - \frac{1}{2}(s_{k,j} - s_{k,i}) + \frac{k s_{k,i} s_{k,j}}{2N_i N_j}(\beta_j N_j + N_j - \beta_i N_i - N_i) = 0. \tag{22}$$

Then, the computation on $s_{k,i}$ can be simplified according to this symmetry.

D. Numerical computations

To demonstrate the variations of $E_u(k)$, $E_{s,i}(k)$, $\Pi_u(k)$, and $\Pi_{s,i}(k)$, a wide range of wavenumbers is required. However, direct computation of Eqs. (18), (20), and (21) in a linear wavenumber space with a wide band, e.g., 50 decades, demands excessive computational resources. Therefore, in this investigation, these computations are performed in a nonlinear wavenumber space by transforming $k = 10^q$, as suggested by Zhao [47]. Considering $\mathrm{d}s_{k,i}/\mathrm{d}k = (10^q \ln 10)^{-1}\mathrm{d}s_{k,i}/\mathrm{d}q$, Eqs. (18), (20), and (21) are converted to

$$F_{ij} = M_i M_j\left[(\ln 10)^{-1}\left(\frac{3}{2} + \frac{2}{N_j}10^q s_{k,j} + \frac{1}{2N_i}10^q s_{k,i}\right)\frac{ds_{k,i}}{dq} + \frac{1}{2}(3\beta_j - 1)s_{k,j} + \frac{\beta_j + 1}{2N_i}10^q s_{k,i}s_{k,j}\right], \tag{23}$$

$$u_k^2 = \sum_{i=1}^{i\max} 10^{(\beta_i - 1)q} M_i s_{k,i}. \tag{24}$$

Equations (20), (23), and (24) (if solvable, see Sec. III D for details) can be numerically solved using the finite difference method, as depicted in Fig. 1. During the computation, the process of the $ds_{k,i}/dq$ term is crucial. Two finite difference schemes have been applied. At a position $q(l)$ with $l > 1$, a first-order approximation was applied with $ds_{k,i}[q(l)]/dq = \{s_{k,i}[q(l)] - s_{k,i}[q(l-1)]\}/\Delta q$, where $\Delta q = q(l) - q(l-1) = 0.006$ is the interval in the q space. When $l \gg 1$, a third-order approximation is applied, with $ds_{k,i}[q(l)]/dq = \{\frac{11}{6}s_{k,i}[q(l)] - 3s_{k,i}[q(l-1)] + \frac{3}{2}s_{k,i}[q(l-2)] - \frac{1}{3}s_{k,i}[q(l-3)]\}/\Delta q$. Since all the $s_{k,i}[q(l-1)]$, $s_{k,i}[q(l-2)]$, and $s_{k,i}[q(l-3)]$ have been solved in previous steps, substituting $ds_{k,i}[q(l)]/dq$ into Eqs. (20) and (23) leaves $s_{k,i}[q(l)]$ as the only unknowns. Equation (23) can be solved based on boundary conditions, $s_{k,i}[q(1)]$. Consequently, $u_k[q(l)]$ can be computed using Eq. (24). The process is then repeated for the next position, $q(l+1)$. Note that in each step, $s_{k,i}$ and u_k each have two solutions, but only one solution can be used in the next calculation. For instance, if solution 2 is picked, it must be used consistently throughout all solving processes. When solution 2 of $s_{k,i}$ and u_k is determined for all q, $s_{k,i}$ and u_k corresponding to solution 2 are obtained for all wavenumbers k. E_u, $E_{s,i}$, Π_u, and $\Pi_{s,i}$ related to solution 2 can be solved according to Eqs. (12a)–(12d).

In the numerical computations for a single scalar, e.g., in Secs. III A and III B, both lower-order and higher-order difference methods were applied for better accuracy. In Sec. III C, where binary scalar components and two coupling mechanisms are concerned, only the lower-order difference method was applied to reduce computation time. All transitions of the subranges, as frequently observed in the following, are natural variations of the solutions of Eqs. (20), (23), and (24), not artificially determined.

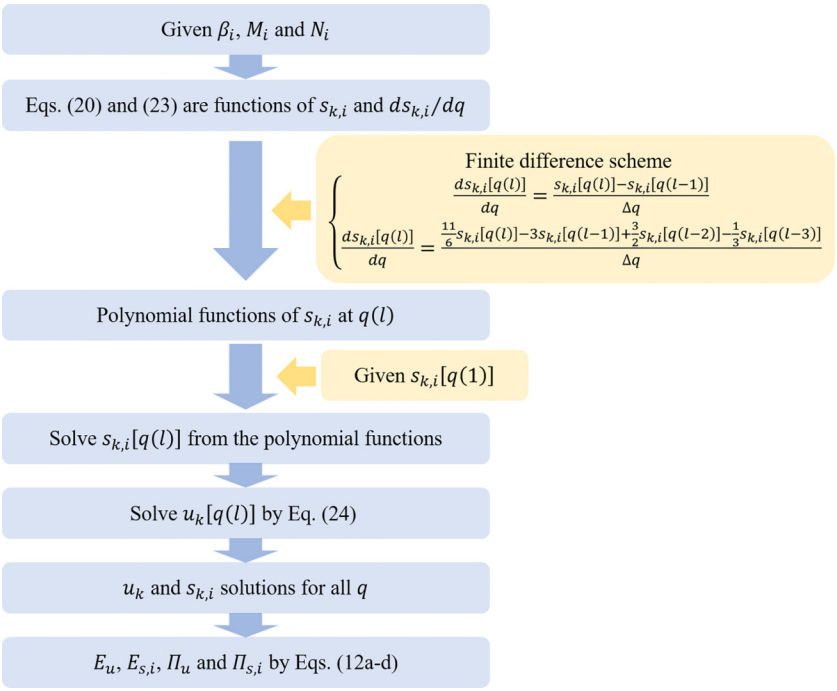

FIG. 1. Flow chart of the procedure in solving $s_{k,i}$, u_k, and the corresponding E_u, $E_{s,i}$, Π_u, and $\Pi_{s,i}$.

III. RESULTS

In this section, we have addressed and resolved several special cases related to the multicomponent model. These cases encompass a range of scenarios. In Sec. III A, a single scalar component with a single coupling mechanism is examined for turbulent systems where there is only one scalar component. For the same problem, Eqs. (18), (20), and (21) are different from that in Zhao's model [47]. Therefore, a comparison between the two models is carried out first to ensure the computation results from the two models are consistent. In Sec. III B, turbulent systems with a single scalar component but subjected to multiple coupling mechanisms, encompassing diverse forms of interactions or forces, have been analyzed. In Sec. III C, turbulent systems consisting of two scalar components where each corresponds to a different coupling mechanism have been investigated. Our analysis centers around understanding the interactions and coupling between these components, and how they impact the overall cascades of the system. In Sec. III D, turbulence systems with three or more scalar components and coupling mechanisms have been preliminarily investigated. Since the features of the inertial subrange have been well established by Kolmogorov, Obukhov, Corrsin, and many researchers, in the following section, this investigation only focuses on the features of MFD subranges.

A. A single scalar component with a single coupling mechanism

Let us begin by considering the simplest case, which involves only a single scalar component and a single coupling mechanism in the model. This scenario is applicable to various models in buoyancy-driven turbulence and EBF-driven turbulence. In buoyancy-driven turbulence, such as thermal convection [32], the control scalar is temperature under the Boussinesq approximation. The coupling between the scalar component and the turbulence occurs through a gravity field. In EBF-driven turbulence, for example, EK turbulence, the control scalar can be either electric conductivity or electric permittivity [34,45], with the coupling mechanism being an electric field. This simplified

scenario captures the essence of these types of turbulent systems, where a single scalar component is influenced by a specific coupling mechanism. Here, $i\max = 1$. Considering $M_1 \neq 0$, Eq. (19) becomes

$$\left(\frac{3}{2}k + \frac{5}{2N_1}k^2 s_{k,1}\right)\frac{ds_{k,1}}{dk} + \frac{3\beta_1 - 1}{2}s_{k,1} + \frac{\beta_1 + 1}{2N_1}k s_{k,1}^2 = 0. \tag{25}$$

This is an alternation of Eq. (17) in Zhao's model [47]. Equation (25) can be rewritten as

$$\frac{ds_{k,1}}{dk} = -\frac{s_{k,1}}{k}\frac{\frac{3\beta_1-1}{2} + \frac{\beta_1+1}{2N_1}k s_{k,1}}{\frac{3}{2} + \frac{5}{2N_1}k s_{k,1}}. \tag{26}$$

From Eq. (26), three different scaling subranges in the MFD subrange can be predicted.

a. Constant-$\mathbf{\Pi_u}$ subrange. When $k s_{k,1} \to 0$, Eq. (26) is simplified as $\frac{ds_{k,1}}{dk} = -\frac{s_{k,1}}{k}\frac{3\beta_1-1}{3}$. Thus, $s_{k,1} \sim k^{\frac{1-3\beta_1}{3}}$, and $u_k \sim M_1 k^{-\frac{1}{3}}$ according to Eq. (18). Thereafter, from Eqs. (12), we simply have $\xi_u = -5/3$, $\xi_{s,1} = -(6\beta_1 + 1)/3$, $\lambda_u = 0$, and $\lambda_{s,1} = (4-6\beta_1)/3$. This corresponds to the constant-Π_u subrange in Zhao's model [47].

b. Constant-$\mathbf{\Pi_s}$ subrange. When $k s_{k,1} \to \infty$, Eq. (26) is simplified as $\frac{ds_{k,1}}{dk} = -\frac{s_{k,1}}{k}\frac{\beta_1+1}{5}$. Thus, $s_{k,1} \sim k^{-\frac{\beta_1+1}{5}}$. According to Eq. (18) and Eqs. (12), $u_k \sim M_1 k^{-\frac{2\beta_1-3}{5}}$, $\xi_u = (4\beta_1 - 11)/5$, $\xi_{s,1} = -(2\beta_1 + 7)/5$, $\lambda_u = (6\beta_1 - 4)/5$, and $\lambda_{s,1} = 0$ are sequentially obtained. This corresponds to the constant-Π_s subrange in Zhao's model [47].

It should be noted that the region where $k s_{k,1} \to 0$ depends on β_1. For $\beta_1 < 4/3$, $k s_{k,1} \to 0$ as $k \to 0$, indicating the constant-Π_u subrange is at the low-wavenumber limit. For $\beta_1 > 4/3$, $k s_{k,1} \to 0$ as $k \to \infty$, indicating the constant-Π_u subrange is at the high-wavenumber limit. For $k s_{k,1} \to \infty$, either $k \to \infty$ for $\beta_1 < 4$, or $k \to 0$ for $\beta_1 > 4$ is required. However, according to Zhao's model [47], $\beta_1 > 4$ leads to a failure of the statistical equilibrium hypothesis, so this situation is not considered in this investigation. Considering the cases together, two different relations between the constant-Π_u subrange and constant-Π_s subrange can be predicted.

For $\beta_1 < 4/3$, the constant-Π_u subrange is located on the lower-wavenumber side of the constant-Π_s subrange. For $4/3 < \beta_1 < 4$, both subranges should be present at the higher-wavenumber side, leading to competition between the two subranges, which may depend on M_1, N_1 and the initial values of $s_{k,1}$. This competition experiences roughly three stages, as numerically investigated by Zhao's model [47]. For $4/3 < \beta_1 < 3/2$, both the constant-Π_u subrange and constant-Π_s subrange are numerically predictable. For $3/2 < \beta_1 < 2$, only the constant-Π_u subrange is observed. For $2 < \beta_1 < 4$, only the constant-Π_s subrange is observed.

c. VF subrange. Beyond the inertial subrange, constant-Π_u subrange, and constant-Π_s subrange, there still exists the fourth subrange where Π_u and Π_s are simultaneously variable, i.e., the VF subrange. This is also a special solution for Eq. (26). When $k s_{k,1} = h N_1$ (h is a real number to be determined), which is a limited number irrelevant to k, it is required that $s_{k,1} = h N_1 k^{-1}$. Equation (26) becomes

$$\frac{\mathrm{d}s_{k,1}}{\mathrm{d}k} = -\frac{s_{k,1}}{k}\frac{3\beta_1 - 1 + (\beta_1 + 1)h}{3 + 5h}. \tag{27}$$

If and only if $h = (3\beta_1 - 4)/(4 - \beta_1)$, Eq. (27) has a solution in the form of $s_{k,1} = h N_1 k^{-1}$. Thus,

$$s_{k,1} = \frac{3\beta_1 - 4}{4 - \beta_1} N_1 k^{-1}. \tag{28}$$

According to Eq. (18) and Eqs. (12), it is easy to get the scaling exponents in the VF subrange as

$$\xi_u = \beta_1 - 3, \quad \xi_{s,1} = -3, \quad \lambda_u = \frac{3}{2}\beta_1 - 2, \quad \lambda_{s,1} = \frac{\beta_1}{2} - 2. \tag{29}$$

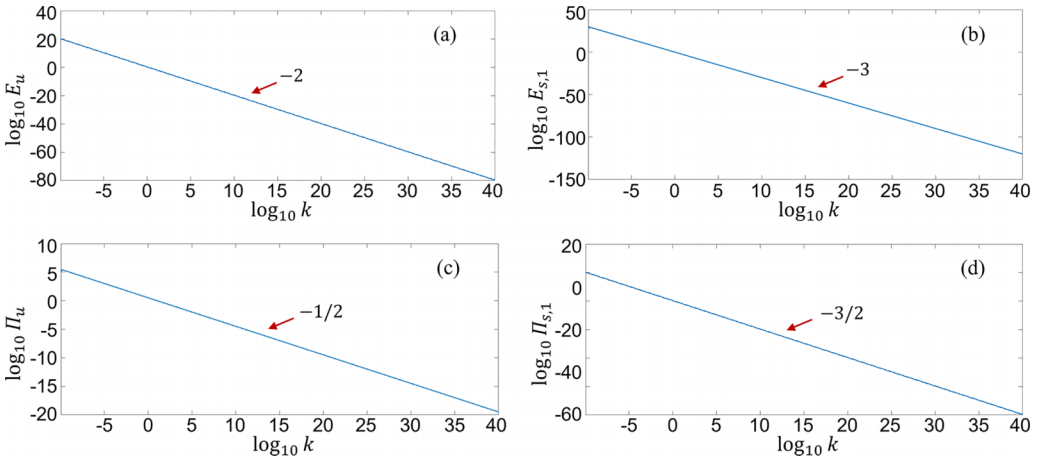

FIG. 2. Spectra of kinetic energy, scalar variance, and their fluxes for the variable flux subrange when $\beta_1 = 1$: (a) $\log_{10}E_u$ vs $\log_{10}k$, (b) $\log_{10}E_{s,1}$ vs $\log_{10}k$, (c) $\log_{10}\Pi_u$ vs $\log_{10}k$, and (d) $\log_{10}\Pi_{s,1}$ vs $\log_{10}k$. It can be seen that $\xi_u = -2$, $\xi_{s,1} = -3$, $\lambda_u = -1/2$, and $\lambda_{s,1} = -3/2$, which are also consistent with the prediction in the VF subrange. Please note that the range of k where the scaling properties emerge has no practical meaning. It strictly relies on the selection of M_1, N_1 and the initial values of $s_{k,1}$. In this case, $M_1 = 1$, $N_1 = 1$, and $s_{k,1} = 1$ are used as an example.

Figure 2 presents an example where $\beta_1 = 1$. By numerically solving Eq. (25) using the method detailed in Sec. II D, the results $\xi_u = -2$, $\xi_{s,1} = -3$, $\lambda_u = -1/2$, and $\lambda_{s,1} = -3/2$ are obtained, which are coincident with the theoretical predictions. Zhao [47] provides another example with $\beta_1 = 0$, demonstrating that either λ_u or $\lambda_{s,1}$ is nonzero, thus supporting the existence of the VF subrange. The theory of the quad-cascade process advanced by Zhao [47] is further validated through a different theoretical approach. For convenience, the scaling exponents for β_1 values of 0 and 1 are summarized in Table I.

When solving Eq. (25), it is important to note the presence of a bifurcation during the transition from the constant-Π_s subrange to the VF subrange as β_1 decreases below 2/3. Figure 3 shows that for $\beta_1 > 2/3$, such as 0.67 and 1, the curves of E_u, $E_{s,1}$, Π_u, and $\Pi_{s,1}$ from the numerical computations are smooth during the transition. However, for $\beta_1 < 2/3$, even at 0.66 which is slightly smaller than 2/3, spikes with equal intervals (in logarithmic coordinates) can be observed in the VF subrange, as shown in Fig. 3. These spikes are independent of the computational resolution

TABLE I. Summary of the scaling exponents of different scaling subranges in a single scalar case, where $\beta_1 = 0$ or 1. The scaling exponents are calculated according to Zhao [47] and Eq. (29) in this investigation.

β_1	Scaling exponents	Inertial subrange	Constant-Π_u subrange	Constant-Π_s subrange	VF subrange
0	ξ_u	$-5/3$	$-5/3$	$-11/5$	-3
	$\xi_{s,i}$	$-5/3$	$-1/3$	$-7/5$	-3
	λ_u	0	0	$-4/5$	-2
	$\lambda_{s,i}$	0	$-4/3$	0	-2
1	ξ_u	$-5/3$	$-5/3$	$-7/5$	-2
	$\xi_{s,i}$	$-5/3$	$-7/3$	$-9/5$	-3
	λ_u	0	0	2/5	$-1/2$
	$\lambda_{s,i}$	0	$-2/3$	0	$-3/2$

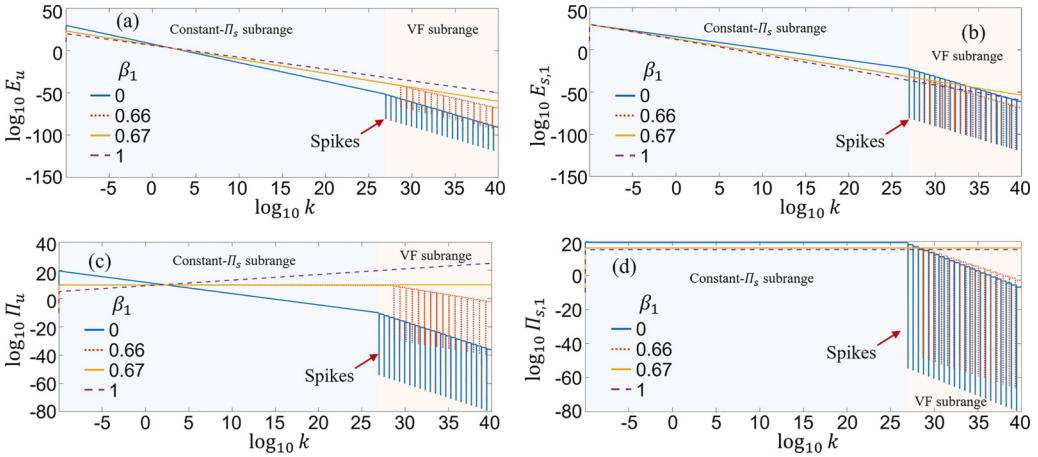

FIG. 3. A bifurcation can be observed during the transition from the constant-Π_s subrange to the VF subrange, even if in a single scalar component situation when β_1 is decreased to below 2/3: (a) $\log_{10}E_u$ vs $\log_{10}k$, (b) $\log_{10}E_{s,1}$ vs $\log_{10}k$, (c) $\log_{10}\Pi_u$ vs $\log_{10}k$, and (d) $\log_{10}\Pi_{s,1}$ vs $\log_{10}k$.

(Δq), suggesting the possible existence of other solution branches when solving the inherently nonlinear and inhomogeneous Eq. (25).

B. A single scalar component with multiple coupling mechanisms

Let us consider another scenario where turbulence is driven by multiple coupling mechanisms, all dependent on a single scalar component (s'). In this case, the energy feeding rate in Eq. (5c) takes the following general form:

$$F_s(\boldsymbol{k}) = \mathrm{Re}[s'(\boldsymbol{k})\boldsymbol{A}(k)\cdot\boldsymbol{u}^*(\boldsymbol{k})], \tag{30}$$

where $\boldsymbol{A}(k) = \sum_{i=1}^{i\max} \boldsymbol{M_i} k^{\beta_i}$ is a modulation function which has a polynomial form of k, with $\beta_i = i-1$. Here, the operator of the multiscale force has the form of $\sum_{i=1}^{i\max} \boldsymbol{M_i}\mathfrak{D}^{(i-1)/4}$. Since N_i is only a function of $\bar{s}_i$, it remains unchanged with i in this case, i.e., $N_i = N$. Besides, let $s'_i = s'$, then Eqs. (3a) and (3b) can be rewritten as

$$\frac{D\boldsymbol{u}}{Dt} = -\frac{1}{\rho}\nabla p + \nu\nabla^2\boldsymbol{u} + \sum_{i=1}^{i\max} \boldsymbol{M_i}\mathfrak{D}^{\frac{(i-1)}{4}} s', \tag{31a}$$

$$\frac{Ds'}{Dt} = -\boldsymbol{N}\cdot\boldsymbol{u} + D_{f,i}\Delta s'. \tag{31b}$$

Accordingly, Eqs. (20), (21), and (18) become

$$\left(\frac{3}{2}k + \frac{5}{2N}k^2 s_k\right)\left(\frac{d}{dk}s_k\right)\sum_{i=1}^{i\max} M_i^2 + \frac{s_k}{2}\sum_{i=1}^{i\max} M_i^2(3i-4) + \frac{k s_k^2}{2N}\sum_{i=1}^{i\max} iM_i^2 = 0, \tag{32}$$

$$u_k^2 = \sum_{i=1}^{i\max} k^{i-2} M_i s_{k,i}. \tag{33}$$

In this section, we discuss two special scenarios to illustrate how multiple coupling mechanisms, even through a single scalar, affect the cascade process of turbulence. One scenario involves turbulence driven by buoyancy and EBF, both caused by variations in the temperature field. The other one considers a modulation function with an exponential form.

1. Turbulence driven by buoyancy and EBF

A typical example is the coexistence of turbulent thermal convection and EK turbulence driven by temperature-dependent electric conductivity. In thermal convection, the flow is driven by temperature fluctuation (T'). In EK turbulence, if electric conductivity fluctuation is caused only by temperature fluctuation, then EK turbulence is driven by the temperature field as well. These two mechanisms strongly couple with each other. For single thermal turbulence convection under the Boussinesq approximation, $i = 1$ (or $\beta_1 = 0$) and $\boldsymbol{M_1} = \alpha \boldsymbol{g}\hat{\boldsymbol{z}}$, where α and g are the thermal expansion coefficient and gravity acceleration, respectively.

For EK turbulence with small electric conductivity variance, if σ is linearly related to temperature fluctuations (T') as $\sigma = \sigma_0 + \frac{\partial \sigma}{\partial T} T'$, with $\sigma_0 = \sigma|_{T=\bar{T}}$, it simply has $\sigma' = \frac{\partial \sigma}{\partial T} T'$. In fluids like water, $\frac{1}{\sigma}\frac{\partial \sigma}{\partial T} = 0.02$ [55,56]. Considering small scalar fluctuations, i.e., $\sigma' \ll \sigma_0$, it is approximately $\frac{\partial \sigma}{\partial T} \approx 0.02\sigma_0$, which is constant within the temperature range. For simplicity, define a constant $\Lambda = \frac{\partial \sigma}{\partial T}$. In EK turbulence, it is approximately $i = 2$ ($\beta_2 = 1$). Therefore, $\mathfrak{D}^{\frac{1}{4}}\sigma' = \Lambda \mathfrak{D}^{\frac{1}{4}} T'$ and $\boldsymbol{M}_2 = -\Lambda \frac{\varepsilon E^2 \hat{\boldsymbol{z}}}{\rho \sigma_0}$.

For this case, $i\mathrm{max} = 2$; then Eqs. (31a) and (31b) can be rewritten as

$$\frac{D\boldsymbol{u}}{Dt} = -\frac{1}{\rho}\nabla p + \nu \nabla^2 \boldsymbol{u} + \boldsymbol{M_1}\mathfrak{D}^0 T' + \boldsymbol{M_2}\mathfrak{D}^{\frac{1}{4}} T', \tag{34a}$$

$$\frac{DT'}{Dt} = -\boldsymbol{N_1} \cdot \boldsymbol{u} + D_{f,1}\Delta T', \tag{34b}$$

$$\frac{D\sigma'}{Dt} = -\boldsymbol{N_2} \cdot \boldsymbol{u} + D_{f,2}\Delta \sigma'. \tag{34c}$$

Here, $\boldsymbol{N_1} = \nabla \bar{T}$ and $\boldsymbol{N_2} = \nabla \bar{\sigma} = \Lambda \nabla \bar{T}$. Equation (34c) becomes

$$\frac{D}{Dt} T' = -\nabla \bar{T} \cdot \boldsymbol{u} + D_{f,2}\Delta T', \tag{35}$$

Thus, the problem involves a single scalar T', but two coupling mechanisms. In the MFD subrange, $D_{f,i}$ has a negligible influence on the cascade processes of turbulent kinetic energy and scalar variance. According to Eqs. (32) and (33), we obtain

$$\left(\frac{3}{2}k + \frac{5}{2N}k^2 s_k\right)\left(\frac{d}{dk}s_k\right)\left[\alpha^2 g^2 + \Lambda^2 \frac{\varepsilon^2 E^4}{\rho^2 \sigma_0^2}\right] + s_k\left[\Lambda^2 \frac{\varepsilon^2 E^4}{\rho^2 \sigma_0^2} - \frac{\alpha^2 g^2}{2}\right] + \frac{1}{2N}\left[\alpha^2 g^2 + 2\Lambda^2 \frac{\varepsilon^2 E^4}{\rho^2 \sigma_0^2}\right] k s_k^2 = 0, \tag{36}$$

$$u_k^2 = \sum_{i=1}^{2} k^{i-2} M_i s_k = \left(\alpha g k^{-1} - \Lambda \frac{\varepsilon E^2}{\rho \sigma_0}\right) s_k. \tag{37}$$

Assuming the working fluid is water, it has $\sigma_0 = 10^{-3}$ S/m and $\Lambda = 2 \times 10^{-5}$ S/m K [55,56]. Let $\alpha = 0.002$ K^{-1} [57], $g = 9.8$ m/s^2, $\rho = 10^3$ kg/m^3, $\varepsilon = 7 \times 10^{-10}$ F/m, $E = 10^2$ V/m, $N = 40$ K/m, $M_1 = 0.02$ m/K s^2 and $M_2 = -\Lambda \frac{\varepsilon E^2}{\rho \sigma_0} = -1.4 \times 10^{-10}$ m^2/K s^2. In this case, $M_1 \gg M_2$, indicating the strength of buoyancy-driven turbulence is much higher than that of EK turbulence. The s_k and u_k can be numerically computed through Eqs. (36) and (37). The results are shown in Fig. 4.

Despite the spikes in solution 1, the entire wavenumber regime can be divided into three subranges from low wavenumber to high wavenumber, including a constant-Π_s subrange of buoyancy-driven turbulence, a new VF subrange that has never been reported, and a VF subrange of EK turbulence. In the constant-Π_s subrange of buoyancy-driven turbulence, the scaling properties align with the BO59 law. The VF subrange corresponding to EK turbulence is also predicted theoretically in Table I. However, in the new VF subrange, new scaling exponents, i.e., $\xi_u = -\frac{6}{5}$, $\xi_{s,1} = -\frac{7}{5}$, $\lambda_u = \frac{7}{10}$, and $\lambda_{s,1} = \frac{1}{2}$, have been observed from the numerical computations, as shown

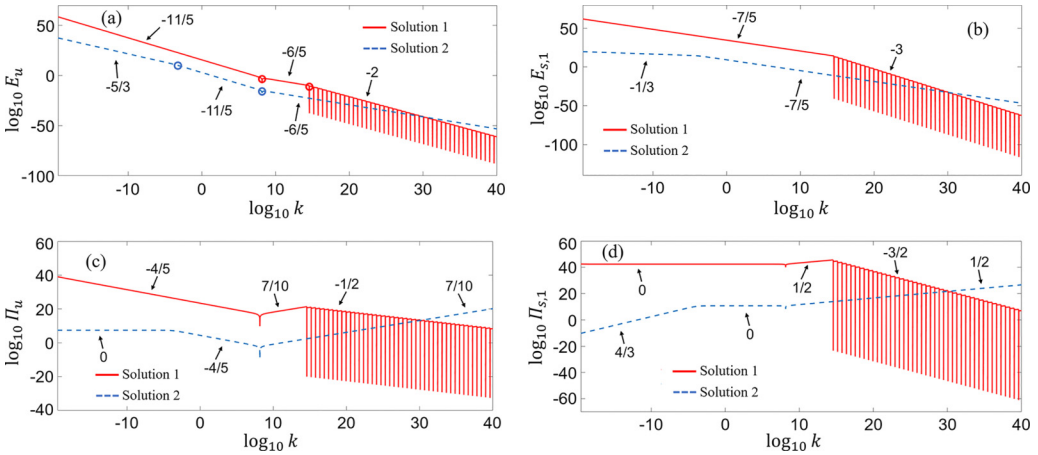

FIG. 4. E_u, $E_{s,1}$, Π_u, and $\Pi_{s,1}$ in the turbulence driven by buoyancy and EBF simultaneously. Here, both solutions 1 and 2 are taken into account. (a) $\log_{10}E_u$ vs $\log_{10}k$, where the red and blue circles represent the intersection positions of different scaling subranges in solution 1 and 2, respectively. (b) $\log_{10}E_{s,1}$ vs $\log_{10}k$. (c) $\log_{10}\Pi_u$ vs $\log_{10}k$. (d) $\log_{10}\Pi_{s,1}$ vs $\log_{10}k$.

in Figs. 4(a)–4(d). In solution 2, there are also three subranges that emerge in sequence, including constant-Π_u and constant-Π_s subranges of buoyancy-driven turbulence, and the new VF subrange observed in solution 1.

The emergence of new VF subranges is a consequence of the entanglement of the two mechanisms, even though $M_1 \gg M_2$ indicates that the strength of EK turbulence is much smaller than that of buoyancy-driven turbulence. This supports that a secondary mechanism can collaborate with the dominant mechanism to significantly influence the cascade processes. When the wavenumber is sufficiently large, even the much weaker influence of EBF can become dominant.

It is important to note that since $\xi_{s,1} = -\frac{7}{5}$ in the new VF subrange is consistent with the BO59 law, careful analysis is required if a $-\frac{7}{5}$ spectrum is observed in such a flow system. The observed $-\frac{7}{5}$ spectrum may not adhere to the BO59 law but to the VF subrange where buoyancy-driven turbulence and EK turbulence coexist.

In Fig. 4(a), the intersection points of the different subranges are plotted. An interesting observation is that the intersection points in solutions 1 and 2 can differ. For instance, in solution 1, the intersection points are located at $k = 10^{8.1}$ and $k = 10^{14.6}$, respectively. In solution 2, the intersection points are located at $k = 10^{-3.2}$ and $k = 10^{8.1}$, respectively. The various intersection points of the different subranges indicate more characteristic scales in turbulence driven by buoyancy and EBF, even though the latter is much weaker than the former.

2. Modulated by an exponential function

In recent years, several investigations have reported on the modulations directly applied to turbulence [58,59]. However, in momentum-scalar coupling turbulence, the coexistence of multiple coupling mechanisms introduces a more complex modulation on the spectra of turbulent kinetic energy and scalar variance. Using the modulation form in Eq. (30), a general modulation model has been established. For instance, if the modulation function takes an exponential form, $\boldsymbol{A}(k) = A_0 e^{-k/C}$ (with C being a reference wavenumber), it can be approximated as $\boldsymbol{A}(k) \approx A_0[1-\frac{k}{C}+\frac{1}{2}(\frac{k}{C})^2-\frac{1}{6}(\frac{k}{C})^3]+O(k^4)$ using a Taylor expansion when $k/C \ll 1$. This approximation is equivalent to having $\beta_i = 0,\ 1,\ 2,\ 3$, with M_i being $1,\ -\frac{1}{C},\ \frac{1}{2C^2}$, and $-\frac{1}{6C^3}$, respectively. Subsequently, s_k and u_k can be solved from Eqs. (32) and (33), as shown in Fig. 5. Here, only one solution is presented.

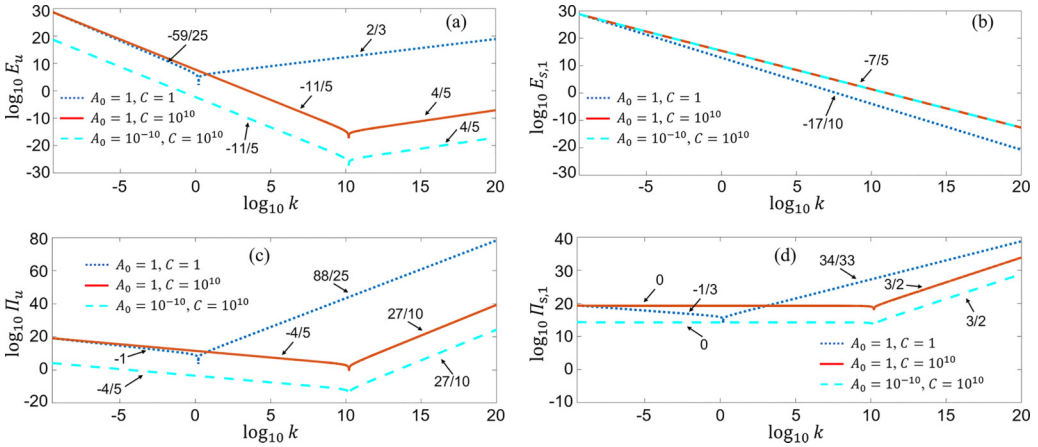

FIG. 5. E_u, $E_{s,1}$, Π_u, and $\Pi_{s,1}$ in the turbulence driven by a single scalar with multiple coupling mechanisms. The modulation function has a form of $\boldsymbol{A}(k) = A_0 e^{-k/C} \approx A_0[1 - \frac{k}{C} + \frac{1}{2}(\frac{k}{C})^2 - \frac{1}{6}(\frac{k}{C})^3]$. Here, only solution 1 is computed. (a) $\log_{10} E_u$ vs $\log_{10} k$, (b) $\log_{10} E_{s,1}$ vs $\log_{10} k$, (c) $\log_{10} \Pi_u$ vs $\log_{10} k$, and (d) $\log_{10} \Pi_{s,1}$ vs $\log_{10} k$.

In the first case, with $A_0 = 1$ and $C = 1$, the M_i values are 1, -1, $\frac{1}{2}$, and $-\frac{1}{6}$, respectively. The small differences among M_i indicate similar forcing intensities among these coupling mechanisms. This scenario demonstrates how multiple mechanisms, rather than a single one, control the cascade process in momentum-scalar coupling turbulence. The cascade process is divided into two new VF subranges intersecting at a wavenumber $k_i = 1.596$, where a singular point is observed in Figs. 5(a), 5(c), and 5(d). In the VF subrange at the lower-wavenumber regime, the scaling exponents are $\xi_u = -59/25$, $\xi_{s,1} = -17/10$, $\lambda_u = -1$, and $\lambda_{s,1} = -1/3$. In the VF subrange at the higher-wavenumber regime, the scaling exponents are $\xi_u = 2/3$, $\xi_{s,1} = -17/10$, $\lambda_u = 88/25$, and $\lambda_{s,1} = 34/33$. These scaling exponents, not predicted in any single scalar component model, strongly depend on the form of $\boldsymbol{A}(k)$, indicating that nonlinear interactions in regimes with multiple coupling mechanisms can lead to unexpected scaling properties. It should be noted that for $k/C > 1$, it is inappropriate to describe the influence of $\boldsymbol{A}(k) = A_0 e^{-k/C}$ modulation using the approximation $\boldsymbol{A}(k) \approx A_0[1 - \frac{k}{C} + \frac{1}{2}(\frac{k}{C})^2 - \frac{1}{6}(\frac{k}{C})^3]$.

In the second case, with $A_0 = 1$ but C increased to 10^{10}, the larger C significantly inhibits the contributions of forcing mechanisms with larger β_i. Consequently, the influence of $\beta_1 = 0$ is promoted, controlling the cascade process. The constant-Π_s subrange and VF subrange of $\beta_1 = 0$ are observed sequentially. Additionally, k_i is postponed to 1.596×10^{10} due to the larger C, indicating a tight relationship between k_i and M_i.

In the third case, where A_0 is changed to 10^{-10} but C is kept at 10^{10}, the cascade process remains the same as in the previous case, differing only in the smaller magnitudes of E_u, Π_u, and $\Pi_{s,1}$ due to the smaller u_k [see Eq. (37)]. The magnitude of A_0 is irrelevant to $E_{s,1}$.

C. Binary scalar components and two coupling mechanisms

In the study of momentum-scalar coupling turbulence, we often encounter scenarios where multiple scalar components and mechanisms can coexist simultaneously. Among these scenarios, binary scalar transport stands out as both a simple and representative example of the complexities involved in multiple scalar transport. This section delves into the cascades of turbulent kinetic energy and scalar variance, driven by binary scalar components that operate independently of each other. This situation is commonly observed in both natural environments and engineering applications.

A notable illustration of this is the simultaneous occurrence of stratified turbulence and EK turbulence. These phenomena are driven by buoyancy and EBF, respectively. The buoyancy force depends on density variations, whereas the EBF is influenced by electric conductivity or permittivity. In instances where density fluctuations are not substantial enough to provoke notable variations in electric conductivity or permittivity, and vice versa, it is logical to treat these quantities as independent from one another. Consequently, density and electric conductivity (or electric permittivity) function as independent scalar quantities, denoted as $s_{k,1}$ and $s_{k,2}$, respectively. These scalar quantities can be addressed and solved using Eq. (18) along with Eqs. (20) and (22), considering a scenario with $i\mathrm{max} = 2$, as

$$M_1^2\left[\left(\frac{3}{2}k+\frac{5}{2N_1}k^2 s_{k,1}\right)\left(\frac{d}{dk}s_{k,1}\right)+\frac{1}{2}(3\beta_1-1)s_{k,1}+\frac{\beta_1+1}{2N_1}ks_{k,1}^2\right]$$
$$+M_2^2\left[\left(\frac{3}{2}k+\frac{5}{2N_2}k^2 s_{k,2}\right)\left(\frac{d}{dk}s_{k,2}\right)+\frac{1}{2}(3\beta_2-1)s_{k,2}+\frac{\beta_2+1}{2N_2}ks_{k,2}^2\right]$$
$$+2M_1M_2\left[\left(\frac{3}{2}k+\frac{2}{N_2}k^2 s_{k,2}+\frac{1}{2N_1}k^2 s_{k,1}\right)\left(\frac{d}{dk}s_{k,2}\right)+\frac{1}{2}(3\beta_2-1)s_{k,2}+\frac{\beta_2+1}{2N_1}ks_{k,1}s_{k,2}\right]=0, \tag{38}$$

$$\frac{3}{2}k\frac{d}{dk}(s_{k,2}-s_{k,1})+k^2\frac{d}{dk}\left(\frac{s_{k,2}^2}{N_2}-\frac{s_{k,1}^2}{N_1}\right)+\left(\frac{1}{2N_1}k^2 s_{k,1}\frac{d}{dk}s_{k,2}-\frac{1}{2N_2}k^2 s_{k,2}\frac{d}{dk}s_{k,1}\right)$$
$$+\frac{3}{2}(\beta_2 s_{k,2}-\beta_1 s_{k,1})-\frac{1}{2}(s_{k,2}-s_{k,1})+\frac{ks_{k,1}s_{k,2}}{2N_1N_2}(\beta_2N_2+N_2-\beta_1N_1-N_1)=0, \tag{39}$$

$$ku_k^2 = k^{\beta_1}M_1 s_{k,1}+k^{\beta_2}M_2 s_{k,2}. \tag{40}$$

In the following sections, some examples of the cascade processes due to binary scalar components will be discussed.

1. A special scenario where $\beta_1 = \beta_2$, $M_1 = M_2$, and $D_{f,1} = D_{f,2}$, but $N_1 \neq N_2$

In this specific scenario, we explore a straightforward example of binary scalar transport, where the two scalar components can be different, yet the underlying driving mechanism across these scalars remains identical. For instance, in EK turbulence, two variants of electric conductivity components (such as Ca^{2+} and Cl^-) with distinct N_1 and N_2 values are incorporated. This results in the equations being approximately defined as $\beta_1 = \beta_2$, $M_1 = M_2$, and $D_{f,1} = D_{f,2}$, although $N_1 \neq N_2$. Consequently, under these assumptions, Eqs. (3b) are reformulated as

$$\frac{Ds_1'}{Dt} = -\boldsymbol{N_1}\cdot\boldsymbol{u}+D_{f,1}\Delta s_1',$$
$$\frac{Ds_2'}{Dt} = -\boldsymbol{N_2}\cdot\boldsymbol{u}+D_{f,1}\Delta s_2'. \tag{41}$$

Any linear combination of s_1' and s_2', defined as $s_c' = as_1' + bs_2'$ (a and b are two proportion coefficients), also fulfills a convection-diffusion equation

$$\frac{Ds_c'}{Dt} = -\boldsymbol{N_c}\cdot\boldsymbol{u}+D_{f,1}\Delta s_c', \tag{42}$$

where $\boldsymbol{N_c} = a\boldsymbol{N_1} + b\boldsymbol{N_2}$. Therefore, theoretically, for the special binary scalar scenario discussed in this section, analyzing s_1' and s_2' should yield results identical to those found in Sec. III A for a single scalar, s_c'. Taking $a = b = 1$ as an example, within the context of a single scalar model and referring to Sec. III A, Eq. (25) can be rewritten as

$$\left(\frac{3}{2}k+\frac{5}{2N_c}k^2 s_{k,c}\right)\frac{ds_{k,c}}{dk}+\frac{3\beta_1-1}{2}s_{k,c}+\frac{\beta_1+1}{2N_c}ks_{k,c}^2=0, \tag{43}$$

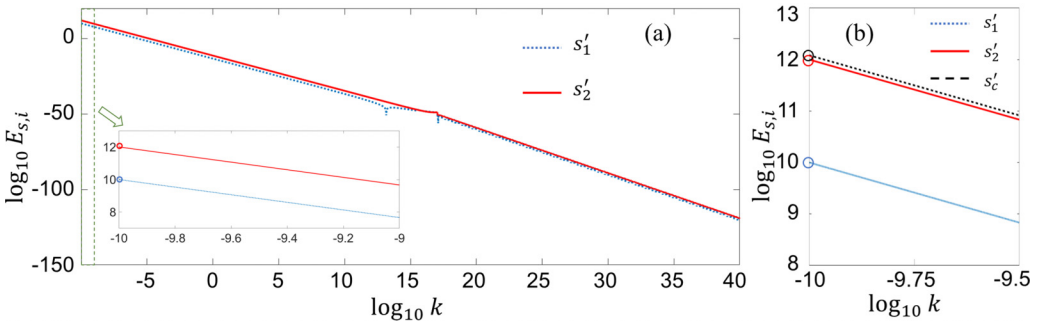

FIG. 6. Spectra of scalar variance at $\beta_1 = 1$. Here, $N_2 = 10N_1$. (a) $\log_{10}E_{s,1}$ and $\log_{10}E_{s,2}$ vary with $\log_{10}k$. $E_{s,1}$ and $E_{s,2}$ are computed from Eqs. (45) and (39). The inset is the zoom-in of the plots. The circles represent the initial values of $E_{s,1}$ and $E_{s,2}$ at the lowest wavenumber. (b) Comparison among the spectra of s_1' and s_2' computed from Eqs. (45) and (39), and s_c' computed from Eq. (43). The circles represent the initial values of $E_{s,1}$, $E_{s,2}$, and $E_{s,c}$ at the lowest wavenumber.

where $s_{k,c} = s_{k,1} + s_{k,2}$ is the spectral component of s_c'. After substituting $s_{k,c}$ and N_c into Eq. (43), it becomes

$$\frac{3}{2}k\frac{d(s_{k,1}+s_{k,2})}{dk} + \frac{5}{2(N_1+N_2)}k^2 s_{k,1}\frac{ds_{k,1}}{dk} + \frac{5}{2(N_1+N_2)}k^2 s_{k,2}\frac{ds_{k,2}}{dk} + \frac{5}{2(N_1+N_2)}k^2 s_{k,1}\frac{ds_{k,2}}{dk} + \frac{5}{2(N_1+N_2)}k^2 s_{k,2}\frac{ds_{k,1}}{dk} + \frac{3\beta_1-1}{2}(s_{k,1}+s_{k,2}) + \frac{\beta_1+1}{2(N_1+N_2)}k\left(s_{k,1}^2 + s_{k,2}^2 + 2s_{k,1}s_{k,2}\right) = 0. \tag{44}$$

When considering binary scalar components s_1' and s_2', according to Eq. (38), the following is obtained:

$$3k\frac{d}{dk}(s_{k,1}+s_{k,2}) + \frac{9}{2N_1}k^2 s_{k,1}\frac{d}{dk}s_{k,1} + \frac{9}{2N_2}k^2 s_{k,2}\frac{d}{dk}s_{k,2} + \frac{1}{2N_1}k^2 s_{k,1}\frac{d}{dk}s_{k,2} + \frac{1}{2N_2}k^2 s_{k,2}\frac{d}{dk}s_{k,1} + (3\beta_1-1)(s_{k,1}+s_{k,2}) + (\beta_1+1)k\left(\frac{s_{k,1}^2}{2N_1} + \frac{s_{k,2}^2}{2N_2}\right) + (\beta_1+1)\left(\frac{N_1+N_2}{2N_1N_2}\right)k s_{k,1}s_{k,2} = 0. \tag{45}$$

Both Eqs. (44) and (45) describe the same phenomenon, indicating they must be either equivalent or proportional. To satisfy this, we introduce the assumption that $s_{k,1}$ and $s_{k,2}$ share the same scaling behavior, differing only by a factor h_c, such that $s_{k,2} = h_c s_{k,1}$. Consequently, Eqs. (44) and (45) are equivalent if $h_c = N_2/N_1$. This leads us to the following relationship:

$$s_{k,2} = \frac{N_2}{N_1}s_{k,1}. \tag{46}$$

In this specific scenario, one can solve for $s_{k,c}$ first. Afterwards, $s_{k,1}$ and $s_{k,2}$ can be calculated using $s_{k,1} = \frac{N_1}{N_1+N_2}s_{k,c}$ and $s_{k,2} = \frac{N_2}{N_1+N_2}s_{k,c}$, respectively. Alternatively, the same results can also be derived by solving Eqs. (39) and (45) directly. Once $s_{k,1}$ and $s_{k,2}$ are obtained, u_k can be calculated through Eq. (40).

Figures 6(a) and 6(b) illustrate further insights. Figure 6(a) showcases the calculated $E_{s,i}$ for $\beta_1 = 1$ and $N_2 = 10N_1$, according to Eqs. (39) and (45). Despite N_2 being an order of magnitude larger than N_1, $E_{s,1}$ and $E_{s,2}$ exhibit remarkably similar distributions, with $E_{s,2} = 10^2 E_{s,1}$ within the constant-Π_u subrange [as shown in the inset of Fig. 6(a)]. In Fig. 6(b), the spectra of s_1', s_2', and s_c' are plotted, derived from Eqs. (45) and (39), and Eq. (43), respectively. Initial values, denoted by circles, reveal $E_{s,c} = E_{s,1} + E_{s,2}$, translating to $s_{k,c} = 11s_{k,1}$ and $s_{k,c} = \frac{11}{10}s_{k,2}$, aligning with the theoretical expectations.

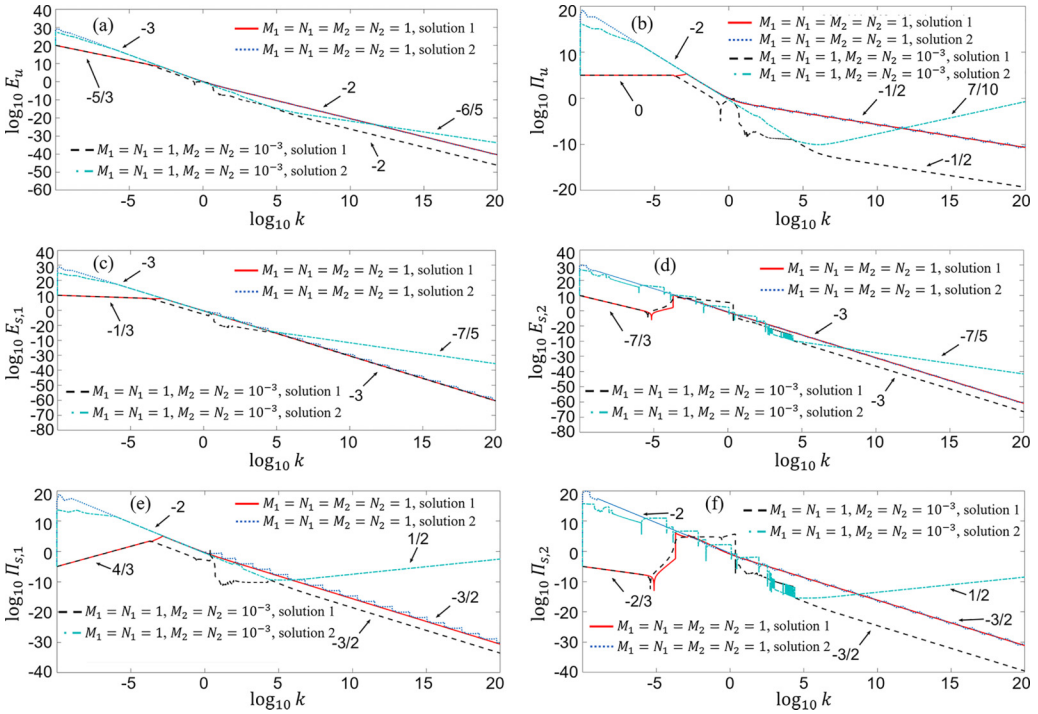

FIG. 7. Spectra computed with binary scalar components at different β_i. Here, $\beta_1 = 0$ and $\beta_2 = 1$ to simulate the turbulence driven by buoyancy and EBF simultaneously. As a conceptual model, the magnitudes of M_i and N_i are selected arbitrarily. (a) $\log_{10}E_u$ vs $\log_{10}k$, (b) $\log_{10}\Pi_u$ vs $\log_{10}k$, (c) $\log_{10}E_{s,1}$ vs $\log_{10}k$, (d) $\log_{10}E_{s,2}$ vs $\log_{10}k$, (e) $\log_{10}\Pi_{s,1}$ vs $\log_{10}k$, and (f) $\log_{10}\Pi_{s,2}$ vs $\log_{10}k$.

This analysis demonstrates that the discussed special scenario can be resolved using either a single or binary scalar component model approach. Furthermore, the model can be extended to incorporate multiple scalar components (for instance, when $i\mathrm{max} > 2$), assuming β_i, M_i, and $D_{f,i}$ remain constant across all components, while N_i varies. Thereafter,

$$s_{k,i} = \frac{N_i}{\sum_i N_i} s_{k,c} \quad \text{and} \quad s_{k,c} = \sum_i s_{k,i}. \tag{47}$$

2. *General scenario of binary scalar components*

In the general scenario involving two binary scalar components, Eqs. (38) and (39) must be solved concurrently to determine $s_{k,1}$ and $s_{k,2}$. Subsequently, u_k is calculated using Eq. (40). Following this, E_u, $E_{s,i}$ ($i = 1, 2$), Π_u, and $\Pi_{s,i}$ can be derived from $s_{k,1}$, $s_{k,2}$, and u_k directly, based on Eqs. (12).

Previous studies have shown that in the wavenumber space, the influence of buoyancy or EBF can be differentiated; buoyancy predominantly affects the cascades in the lower wavenumber ranges, while EBF governs the higher wavenumber ranges. However, the interaction between these mechanisms in a regime where both are present remains unclear. This section explores the combined effects of buoyancy ($\beta_1 = 0$) and EBF ($\beta_2 = 1$) with varying strengths on the cascades of turbulent kinetic energy and scalar variance. The two scalar components considered could represent temperature and electric conductivity, respectively.

Figure 7 illustrates the wavenumber subranges influenced by both buoyancy and EBF. In a conceptual model setting, the magnitudes of M_i and N_i were arbitrarily chosen. With $M_1 = M_2 = 1$

and $N_1 = N_2 = 1$ as an example, solution 1 (depicted by red lines) shows a sequence of a constant-Π_u subrange followed by two VF subranges. In the constant-Π_u subrange, located in the lower-wavenumber regime, $\xi_u = -\frac{5}{3}$ [Fig. 7(a)] and $\lambda_u = 0$ [Fig. 7(b)], $\xi_{s,1} = -\frac{1}{3}$ [Fig. 7(c)], $\xi_{s,2} = -\frac{7}{3}$ [Fig. 7(d), $\lambda_{s,1} = \frac{4}{3}$ [Fig. 7(e)], and $\lambda_{s,2} = -\frac{2}{3}$ [Fig. 7(f)], which are aligning with single scalar predictions in Table I for $\beta_1 = 0$ and $\beta_2 = 1$, respectively.

Following the constant-Π_u subrange is a VF subrange driven by buoyancy, where $\xi_u = -3$, $\xi_{s,1} = \xi_{s,2} = -3$, $\lambda_u = -2$, and $\lambda_{s,1} = \lambda_{s,2} = -2$. In this subrange, EBF plays a negligible role, and the cascades of s_2' are the same as those of s_1'. Proceeding to the higher-wavenumber side, another VF subrange completely governed by EBF is visible, where the influence of buoyancy is negligible, and $\xi_u = -2$, $\xi_{s,1} = \xi_{s,2} = -3$, $\lambda_u = -\frac{1}{2}$, and $\lambda_{s,1} = \lambda_{s,2} = -\frac{3}{2}$ which are coincident to Table I as well.

When considering a scenario where the second mechanism is weaker ($M_2 = 10^{-3}$ and $N_2 = 10^{-3}$), solution 1 (depicted by black dashed lines) presents two distinct subranges. One is the constant-Π_u subrange located at the lower-wavenumber regime attributed to buoyancy, and the other is the VF subrange located at the higher-wavenumber regime attributed to EBF. According to the unbalanced forcing through buoyancy and EBF, the VF subrange of buoyancy-driven turbulence mentioned in the previous paragraph is not observed in this case. Instead, a highly fluctuated transitional regime is present, where singular and intermittent (sudden fall) spectra are numerically computed [see, e.g., Figs. 7(b) and 7(d)–7(f)]. Despite the reduced magnitudes of M_2 and N_2, their effect on the overall scaling in the constant-Π_u subrange dominated by buoyancy remains unchanged. In the VF subrange dominated by EBF, the values of E_u, $E_{s,i}$ ($i = 1, 2$), Π_u, and $\Pi_{s,i}$ are all significantly lower than those in the previous scenario, as illustrated in Fig. 7. Yet, an intriguing exception is observed: smaller values of M_2 and N_2 lead to a reduction in $\Pi_{s,1}$ within this subrange, without impacting $E_{s,1}$. Such a phenomenon is not observed in conventional hydrodynamic turbulence. Nonetheless, in turbulence that involves momentum-scalar coupling, this behavior may be more common. This is because $\Pi_{s,i}$ [as defined in Eq. (12d)] are more influenced by the smaller M_2, mediated through u_k [Eq. (18)].

The impact of solution 2 on the previously mentioned scenarios has also been examined, with findings presented in Fig. 7. Analyzing the spectra indicated by blue dotted lines, when $M_1 = M_2 = 1$ and $N_1 = N_2 = 1$, the cascade divides into two distinct subranges. The first is a VF subrange of buoyancy-driven turbulence found in the lower-wavenumber regime. The second subrange, situated in the higher-wavenumber region, pertains to EK turbulence. Despite the appearance of a "zigzag" pattern in this higher subrange [as seen in Figs. 7(b), 7(e), and 7(f)], the overall trend aligns with the predictions for the VF subrange of EK turbulence detailed in Table I.

Conversely, when implementing solution 2 with $M_1 = 1$, $N_1 = 1$, $M_2 = 10^{-3}$, and $N_2 = 10^{-3}$ (represented by blue dot-dashed lines), novel scaling characteristics emerge. In the lower-wavenumber regime, the VF subrange for buoyancy-driven turbulence remains noticeable. Yet, within the higher-wavenumber sphere, the new VF subrange—previously discussed in Sec. III B—emerges again, characterized by $\xi_u = -\frac{6}{5}$, $\xi_{s,1} = \xi_{s,2} = -\frac{7}{5}$, $\lambda_u = \frac{7}{10}$, and $\lambda_{s,1} = \lambda_{s,2} = \frac{1}{2}$.

These observations underscore the nuanced interplay between buoyancy and EBF in turbulence, suggesting that a variety of scaling behaviors can emerge based on the relative strengths of these mechanisms. This complexity invites further investigation, particularly in scenarios with more varied magnitudes of M_i and N_i, indicating the potential for uncovering additional unpredictable scalings in momentum-scalar coupling turbulence.

D. Three or more scalar components

When there are three or more independent scalar components, that is, $i\max \geqslant 3$, solving for the $i\max + 1$ unknowns (u_k and $s_{k,i}$) using the given equations $[(i\max^2 - i\max)/2 + 2]$ from Eqs. (18), (20), and (21) leads to a nonclosure issue. The problem appears overdetermined at first glance because there are more equations than unknowns, making the determination of the solutions exceedingly challenging. However, in a physical system, such as EK turbulence involving more than three electrolyte components (e.g., Na^+, K^+, Ca^{2+}, Mg^{2+}, Cl^-, and others), deterministic

solutions for u_k and $s_{k,i}$ should exist and be experimentally measurable. This suggests that, in reality, the solutions should be unique and attainable. Therefore, it can be deduced that there are $(i\max^2 - 3i\max)/2 + 1$ constraints necessary to make the equations solvable.

Identifying these unknown constraints is vital for comprehending complex nonlinear systems with multiple components and coupling mechanisms, which are more applicable to real-world situations than the highly simplified models like K41 [53], the Bolgiano-Obukhov model [26,27], the Zhao-Wang model [34], etc. A prime example is in electrochemical engineering, where the mixture of complex chemical components in a turbulent mixer with the presence of EK flow facilitates chemical reactions. Knowing the exact spatial or spectral distribution of each chemical component is crucial to predicting the reaction outcomes. Nevertheless, this topic exceeds the current study's scope and will be addressed in future research.

IV. CONCLUSIONS

This study introduces a theoretical model for the cascade processes in momentum-scaling coupling turbulence driven by multiple scalar components and various mechanisms, building upon the general flux model proposed by Zhao [47]. The current model comprehensively supports the quad-cascade processes of turbulent kinetic energy and scalar variance, while also forecasting new scaling properties.

For a model with a single scalar component where only one coupling mechanism is taken into account, it predicts that the variable flux subrange can exhibit scaling exponents $\xi_u = \beta_1 - 3$, $\xi_{s,1} = -3$, $\lambda_u = \frac{3}{2}\beta_1 - 2$, and $\lambda_{s,1} = \frac{1}{2}\beta_1 - 2$, derived from the order of deviation in the multiscale force $\boldsymbol{M}_i \mathfrak{D}^{\beta_i/4} s_i'$. Remarkably, spikes are identified in the variable flux subranges when $\beta_i < 2/3$, suggesting the emergence of local intermittency when solving the inherently nonlinear and inhomogeneous conservation equation.

In the context of turbulence driven by a single scalar but subjected to multiple coupling mechanisms, for instance, the combined effects of buoyancy-driven turbulence and EK turbulence due to temperature variations, a distinctive variable flux subrange is detected. This subrange exhibits scaling exponents $\xi_u = -\frac{6}{5}$, $\xi_{s,1} = -\frac{7}{5}$, $\lambda_u = \frac{7}{10}$, and $\lambda_{s,1} = \frac{1}{2}$. With the expansion of this model to include an exponential modulation function, the emergence of two new variable flux subranges is disclosed. The first, in the lower-wavenumber regime, displays scaling exponents $\xi_u = -\frac{59}{25}$, $\xi_{s,1} = -\frac{17}{10}$, $\lambda_u = -1$, and $\lambda_{s,1} = -\frac{1}{3}$. The second appears in the higher-wavenumber regime, marked by scaling exponents $\xi_u = \frac{2}{3}$, $\xi_{s,1} = -\frac{17}{10}$, $\lambda_u = \frac{88}{25}$, and $\lambda_{s,1} = \frac{34}{33}$. These findings reveal that the determined scaling exponents heavily rely on the chosen modulation function. Moreover, it hints at the potential to manipulate the scaling properties and cascade processes by strategically aligning different scalar components and coupling mechanisms.

Subsequently, this study delves into a binary scalar components model, specifically focusing on electrokinetic turbulence ($\beta_i = 1$) driven by two types of ions with disparate mean concentration gradients. Two approaches are compared: one using a single scalar component model based on the linear relationship between the two scalar transport equations, and the other directly computing the cascade process using the binary scalar component model. These distinct approaches both converge on the same outcomes regarding the cascade processes, indicating consistency in the results derived from simplified and more complex models.

Further exploration into the interplay between buoyancy-driven turbulence ($\beta_1 = 0$) and electrokinetic turbulence ($\beta_2 = 1$), characterized by temperature and electric conductivity as the two scalar components, reveals that the cascade process is comprised of several distinct subranges, including the constant-Π_u subrange, VF subranges of buoyancy-driven turbulence and EK turbulence, etc. Notably, the new variable flux subrange characterized by $\xi_u = -\frac{6}{5}$, $\xi_{s,1} = \xi_{s,2} = -\frac{7}{5}$, $\lambda_u = \frac{7}{10}$, and $\lambda_{s,1} = \lambda_{s,2} = \frac{1}{2}$ is observed again. This finding is further corroborated by using the single-scalar-component model influenced by dual mechanisms.

The investigation then addresses the complexities that arise when three or more distinct scalar components and coupling mechanisms simultaneously coexist, leading to potentially overdetermined conservative equations. Yet, from a physical standpoint, it is posited that unique solutions for the cascades of multiple scalars, which can be empirically validated, must exist. It suggests that additional equations or constraints are needed to circumvent these complexities, setting the stage for further research endeavors.

Turbulence is a complex and challenging phenomenon, particularly in the context of momentum-scalar coupling, where multiple scalar components and coupling mechanisms come into play. Despite its importance, the cascade process of momentum-scalar coupling turbulence has received limited attention and remains poorly understood. In this study, we have undertaken an effort to address this knowledge gap and shed light on a small part of this complex problem, which is bound to be confronted sooner or later. By doing so, we aim to uncover the diverse scaling properties observed experimentally in momentum-scalar coupling turbulence, including phenomena in buoyancy-driven turbulence in the atmosphere. Understanding the cascade processes and scaling properties in these turbulent flows is crucial for various scientific fields, not only for the conventional hydrodynamic turbulence, but also for theoretical physics and optics [60,61], particularly in wave turbulence [62,63] when more complex coupling of multiple wave functions must be included. Our findings contribute to the groundwork necessary for future investigations and deepen our understanding of turbulent flows across different physical systems.

ACKNOWLEDGMENT

This investigation is supported by National Natural Science Foundation of China (Grant No. 51927804).

The author reports no conflict of interest.

[1] H. Jiang, X. Zhu, D. Wang, S. G. Huisman, and C. Sun, Supergravitational turbulent thermal convection, Sci. Adv. **6**, eabb8676 (2020).

[2] H. Zhang and Y.-H. Zhou, Unveiling the spectrum of electro-hydrodynamic turbulence in dust storms, Nat. Commun. **14**, 408 (2023).

[3] B. Knaepen and R. Moreau, Magnetohydrodynamic turbulence at low magnetic Reynolds number, Annu. Rev. Fluid Mech. **40**, 25 (2008).

[4] G. Eyink, E. Vishniac, C. Lalescu, H. Aluie, K. Kanov, K. Burger, R. Burns, C. Meneveau, and A. Szalay, Flux-freezing breakdown in high-conductivity magnetohydrodynamic turbulence, Nature (London) **497**, 466 (2013).

[5] L. Madeira, M. A. Caracanhas, F. E. A. d. Santos, and V. S. Bagnato, Quantum turbulence in quantum gases, Annu. Rev. Condens. Matter Phys. **11**, 37 (2020).

[6] J. T. Mäkinen, S. Autti, P. J. Heikkinen, J. J. Hosio, R. Hänninen, V. S. L'vov, P. M. Walmsley, V. V. Zavjalov, and V. B. Eltsov, Rotating quantum wave turbulence, Nat. Phys. **19**, 898 (2023).

[7] R. Alert, J. Casademunt, and J.-F. Joanny, Active turbulence, Annu. Rev. Condens. Matter Phys. **13**, 143 (2022).

[8] G. Ahlers, S. Grossmann, and D. Lohse, Heat transfer and large scale dynamics in turbulent Rayleigh-Bénard convection, Rev. Mod. Phys. **81**, 503 (2009).

[9] J. J. Niemela, L. Skrbek, K. R. Sreenivasan, and R. J. Donnelly, Turbulent convection at very high Rayleigh numbers, Nature (London) **404**, 837 (2000).

[10] P. A. Davidson, *Turbulence in Rotating, Stratified and Electrically Conducting Fluids* (Cambridge University Press, New York, 2013).

[11] Y. Fan, E. Jarosz, Z. Yu, W. E. Rogers, T. G. Jensen, and J.-H. Liang, Langmuir turbulence in horizontal salinity gradient, Ocean Modell. **129**, 93 (2018).

[12] G. Wang, F. Yang, and W. Zhao, There can be turbulence in microfluidics at low Reynolds number, Lab Chip **14**, 1452 (2014).
[13] G. Wang, F. Yang, and W. Zhao, Microelectrokinetic turbulence in microfluidics at low Reynolds number, Phys. Rev. E **93**, 013106 (2016).
[14] G. Wang, F. Yang, W. Zhao, and C.-P. Chen, On micro-electrokinetic scalar turbulence in microfluidics at low Reynolds number, Lab Chip **16**, 1030 (2016).
[15] A. Varshney, S. Gohil, M. Sathe, S. R. R. V, J. B. Joshi, S. Bhattachary, A. Yethiraj, and S. Ghosh, Multiscale flow in an electro-hydrodynamically driven oil-in-oil emulsion, Soft Matter **12**, 1759 (2016).
[16] W. Zhao and G. Wang, Cascade of turbulent energy and scalar variance in DC electrokinetic turbulence, Physica D **399**, 42 (2019).
[17] K. Kitazawa, Y. Ikezoe, H. Uetake, and N. Hirota, Magnetic field effects on water, air and powders, Physica B **294**, 709 (2001).
[18] Y. Kuramoto, *Diffusion-Induced Chemical Turbulence* (Springer, Berlin, 1980).
[19] S. B. Pope, PDF methods for turbulent reactive flows, Prog. Energy Combust. Sci. **11**, 119 (1985).
[20] H. Kikuchi, EHD turbulence, vortices, and self-organizations, in *Electrohydrodynamics in Dusty and Dirty Plasmas* (Springer, Dordrecht, 2001), pp. 140–160.
[21] M. El-Alaoui, R. J. Walker, J. M. Weygand, G. Lapenta, and M. L. Goldstein, Magnetohydrodynamic turbulence in the earth's magnetotail from observations and global MHD simulations, Front. Astron. Space Sci. **8**, 620519 (2021).
[22] Y. He, S. Sun, D. Y. Kim, B. G. Jang, H. Li, and H.-k. Mao, Superionic iron alloys and their seismic velocities in Earth's inner core, Nature (London) **602**, 258 (2022).
[23] B. A. Perry and M. E. Mueller, Joint probability density function models for multiscalar turbulent mixing, Combust. Flame **193**, 344 (2018).
[24] M. Lesieur, *Turbulence in Fluids* (Springer, Dordrecht, 2008).
[25] A. M. Obukhov, Structure of the temperature field in turbulent flow, Translation Izvestiia Akademii Nauk S.S.S.R., Ser. Geogr. i Geofiz. **XIII**, 58 (1949).
[26] R. Bolgiano, Turbulent spectra in a stably stratified atmosphere, J. Geophys. Res. **64**, 2226 (1959).
[27] A. M. Obukhov, Effect of Archimedean forces on the structure of the temperature field in a turbulent flow, Dokl. Akad. Nauk. SSSR **125**, 1246 (1959).
[28] D. Lohse and K.-Q. Xia, Small-scale properties of turbulent Rayleigh-Bénard convection, Annu. Rev. Fluid Mech. **42**, 335 (2010).
[29] A. Kumar, A. G. Chatterjee, and M. K. Verma, Energy spectrum of buoyancy-driven turbulence, Phys. Rev. E **90**, 023016 (2014).
[30] A. Kumar and M. K. Verma, Shell model for buoyancy-driven turbulence, Phys. Rev. E **91**, 043014 (2015).
[31] D. Wang, S. Liu, Q. Zhou, and C. Sun, Spectra and structure functions of the temperature and velocity fields in supergravitational thermal turbulence, Phys. Fluids **34**, 055108 (2022).
[32] M. K. Verma, A. Kumar, and A. Pandey, Phenomenology of buoyancy-driven turbulence: Recent results, New J. Phys. **19**, 025012 (2017).
[33] S. Alam, A. Guha, and M. K. Verma, Revisiting Bolgiano–Obukhov scaling for moderately stably stratified turbulence, J. Fluid Mech. **875**, 961 (2019).
[34] W. Zhao and G. Wang, Scaling of velocity and scalar structure functions in ac electrokinetic turbulence, Phys. Rev. E **95**, 023111 (2017).
[35] W. Zhao, W. Su, and G. Wang, Interactions of velocity structures between large and small scales in microelectrokinetic turbulence, Phys. Rev. Fluids **6**, 074610 (2021).
[36] P. S. Iroshnikov, Turbulence of a conducting fluid in a strong magnetic field, Sov. Astron. **7**, 566 (1964).
[37] R. H. Kraichnan, Inertial-range spectrum of hydromagnetic turbulence, Phys. Fluids **8**, 1385 (1965).
[38] D. Biskamp, *Magnetohydrodynamic Turbulence* (Cambridge University Press, Cambridge, UK, 2003).
[39] A. Chepurnov and A. Lazarian, Extending the big power law in the sky with turbulence spectra from Wisconsin Ha Mapper data, Astrophys. J. **710**, 853 (2010).
[40] R. J. Leamon, C. W. Smith, N. F. Ness, W. H. Matthaeus, and H. K. Wong, Observational constraints on the dynamics of the interplanetary magnetic field dissipation range, J. Geophys. Res. **103**, 4775 (1998).

[41] M. K. Verma, Statistical theory of magnetohydrodynamic turbulence: Recent results, Phys. Rep. **401**, 229 (2004).
[42] M. K. Verma, Variable energy flux in turbulence, J. Phys. A Math. Theor. **55**, 013002 (2022).
[43] S. Strogatz, S. Walker, J. M. Yeomans, C. Tarnita, E. Arcaute, M. D. Domenico, O. Artime, and K.-I. Goh, Fifty years of "More is different", Nat. Rev. Phys. **4**, 508 (2022).
[44] P. W. Anderson, More is different, Science **177**, 393 (1972).
[45] W. Zhao and G. Wang, A tentative study of the transport of energy and other scalar quantities in forced turbulence driven by ∇^n A-type volume forces, J. Hydrodyn. Ser. B (English Ed.) **33**, 1271 (2021).
[46] S. Basu and A. A. M. Holtslag, Revisiting and revising Tatarskii's formulation for the temperature structure parameter (C_T^2) in atmospheric fows, Environ. Fluid Mech. **22**, 1107 (2022).
[47] W. Zhao, General flux model in the turbulence driven by multiscale forces, Phys. Rev. Fluids **7**, 084607 (2022).
[48] R. K. Zeytounian, Joseph Boussinesq and his approximation: A contemporary view, C. R. Mec. **331**, 575 (2003).
[49] D. Nath, A. Pandey, A. Kumar, and M. K. Verma, Near isotropic behavior of turbulent thermal convection, Phys. Rev. Fluids **1**, 064302 (2016).
[50] P. A. Davidson, *Turbulence: An Introduction for Scientists and Engineers* (Oxford Univesity Press, New York, 2004).
[51] M. K. Verma, *Physics of Buoyant Flows: From Instabilities to Turbulence* (World Scientific, Singapore, 2018).
[52] U. Frisch, *Turbulence—The legacy of A. N. Kolmogorov* (Cambridge University Press, New York, 1995).
[53] A. N. Kolmogorov, The local structure of turbulence in imcompressible viscous fluid for very large Reynolds numbers, Dokl. Akad. Nauk SSSR **30**, 301 (1941).
[54] S. Corrsin, On the spectrum of isotropic temperature fluctuations in an isotropic turbulence, J. Appl. Phys. **22**, 469 (1951).
[55] D. R. Lide, *CRC Handbook of Chemistry and Physics*, 90th ed. (CRC Press/Taylor and Francis, Boca Raton, FL, 2009).
[56] A. Ramos, H. Morgan, N. G. Green, and A. Castellanos, AC electrokinetics: A review of forces in microelectrode structures, J. Phys. D Appl. Phys. **31**, 2338 (1998).
[57] N. M. Putintsev and D. N. Putintsev, Heat capacity and thermal expansion of water and helium, J. Therm. Sci. **26**, 125 (2017).
[58] J. K. Bhattacharjee, A randomly stirred model for Bolgiano–Obukhov scaling in turbulence in a stably stratified fluid, Philos. Trans. R. Soc. A **380**, 20210075 (2022).
[59] C. DeDominicis and P. C. Martin, Energy spectra of certain randomly stirred fluids, Phys. Rev. A **19**, 419 (1979).
[60] M. Al-Mahmoud, V. Coda, A. Rangelov, and G. Montemezzani, Non-Hermitian quantum-like cascaded nonlinear optical frequency conversion and splitting in dissipative media, J. Phys. B **55**, 184005 (2022).
[61] Y. Tang, K. Li, X. Zhang, J. Deng, G. Li, and E. Brasselet, Harmonic spin–orbit angular momentum cascade in nonlinear optical crystals, Nat. Photonics **14**, 658 (2020).
[62] S. Nazarenko, *Wave Turbulence* (Springer, Heidelberg, 2011).
[63] Y. Zhu, B. Semisalov, G. Krstulovic, and S. Nazarenko, Self-similar evolution of wave turbulence in Gross-Pitaevskii system, Phys. Rev. E **108**, 064207 (2023).